



Contents lists available at ScienceDirect

Remote Sensing of Environment

journal homepage: www.elsevier.com/locate/rse

Surface response and subsurface features during the restriction of groundwater exploitation in Suzhou (China) inferred from decadal SAR interferometry

Guoqiang Shi ^a, Peifeng Ma ^{a,f,*}, Xie Hu ^{c,d,1}, Bo Huang ^{a,e,*}, Hui Lin ^b

^a Institute of Space and Earth Information Science, The Chinese University of Hong Kong, Shatin, N.T., Hong Kong

^b Key Lab of Poyang Lake Wetland and Watershed Research of Ministry of Education, School of Geography and Environment, Jiangxi Normal University, Nanchang 330022, China

^c Berkeley Seismological Laboratory, University of California, Berkeley, CA 94720-4767, USA

^d Department of Earth and Planetary Science, University of California, Berkeley, CA 94720-4767, USA

^e Department of Geography and Resource Management, The Chinese University of Hong Kong, Shatin, N.T., Hong Kong

^f Shenzhen Research Institute, The Chinese University of Hong Kong, Shenzhen 518063, China

ARTICLE INFO

Keywords:

Groundwater overexploitation
Aquifer deformation
Geological boundary
Restrictions on groundwater exploitation (RGE)
InSAR

ABSTRACT

Groundwater overexploitation has caused dramatic land subsidence over the metropolitan areas in the Yangtze River Delta (YRD) and many other economic centers worldwide. Suzhou (China) is such a sinking city and faces enhanced flood risks. Restrictions on groundwater exploitation (RGE) have been imposed by the government since 1997 to prevent further elevation loss. However, knowledge on the spatiotemporal evolution of the urban land deformation during the RGE is limited by sparse and infrequent field measurements, which may bias the evaluation of the RGE policy and the strategy formulation of water management. Interferometric synthetic aperture radar (InSAR) provides regional surface deformation at a regular temporal interval of dozens of days. Here we present the decadal evolution of ground deformation in Suzhou using multiple InSAR datasets from ERS1/2, ENVISAT-ASAR, and ALOS-1 PALSAR-1 during 1993–2010, spanning the entire RGE period. An elongated zone from southern to northwestern Suzhou is highlighted by a drastic cumulative land subsidence exceeding 0.9 m due to inelastic aquifer compaction. We characterize the spatiotemporal ground deformation response to the RGE policy using an exponential decay function, from which we also infer the subsurface boundaries with sharp bedrock gradients. We identify a corridor connecting the Yangcheng and Taihu lakes, which is highly sensitive to RGE during the decelerated subsidence. Our analysis also suggests that urban subsidence in Suzhou was under control by $2006_{-0.4}^{+1.4}$.

1. Introduction

Groundwater is the water supply for civilian use, agricultural irrigation, and industrial production in cities built on unconfined or semi-confined aquifers (Foster et al., 1999; Foster, 2001). Land subsidence caused by groundwater depletion is a common issue in many countries worldwide (Pacheco-Martínez et al., 2013). In China, groundwater used to be freely extracted to meet the high demand of industrial production and municipal use since the 1970s (Hu et al., 2004; Huang et al., 2014). The associated land subsidence by over-pumping occurred in many

emerging cities surrounding the Yangtze River Delta (YRD) (Shi et al., 2008a; Wu et al., 2008; Wu et al., 2009), the North China Plain (NCP) (Guo et al., 2015; Gong et al., 2018), and the Fenwei Plain (FP) (Wang et al., 2019). Suzhou, a representative industrial center in the YRD, was subsiding seriously due to a drastic decrease in groundwater level from the 1980s to the end of 20th century (Huang and Zhou, 2011; Shi et al., 2012). The continuous decline of groundwater level often results in the irreversible compaction of the aquifer system and permanent surface settlement (Hoffmann et al., 2003), such as Mexico City (Osmanoğlu et al., 2011; Chaussard et al., 2014b) and the nationwide subsidence of

* Corresponding authors at: Institute of Space and Earth Information Science, The Chinese University of Hong Kong, Shatin, N.T., Hong Kong.

E-mail addresses: guoqiang.shi@link.cuhk.edu.hk (G. Shi), mapeifeng@cuhk.edu.hk (P. Ma), xiehu@uh.edu (X. Hu), bohuang@cuhk.edu.hk (B. Huang), huilin@cuhk.edu.hk (H. Lin).

¹ Current address: Department of Civil and Environmental Engineering, University of Houston, Houston, TX, USA.

<https://doi.org/10.1016/j.rse.2021.112327>

Received 27 March 2020; Received in revised form 4 November 2020; Accepted 30 January 2021

Available online 12 February 2021

0034-4257/© 2021 Elsevier Inc. All rights reserved.

Indonesia (Chaussard et al., 2013). Land subsidence is risky especially in the densely populated and lower-altitude delta areas, and it requires a safety monitoring network (Hu et al., 2004; van der Horst et al., 2018). Multiple geological hazards may result from land subsidence such as flooding (e.g., the catastrophic 1999 Taihu Basin flood in Suzhou) (Wu, 2000; Wang et al., 2011), earth fissures (Wang et al., 2009; Ye et al., 2018), surficial and shallow infrastructure damage (Ng et al., 2013; Abidin et al., 2015), and permanent compaction (Shi et al., 2012). Urban subsidence was first documented in the Suzhou-Wuxi-Changzhou (SWC) city group in the 1960s (Wu et al., 2009). Mitigation measures were taken to restrict groundwater exploitation from 1995; however, considerable pumping continued and varied in different counties (Shi et al., 2012). By the end of the 20th century, the average cumulative subsidence was >1 m in SWC and even >2 m in some local sites (Sun, 2002; Xue et al., 2005; Wu et al., 2009). In 1997, the Jiangsu government started the restrictions on groundwater exploitation (RGE) over the entire SWC city group. More stringent laws from 2000 decelerated groundwater exploitation progressively, and an overall ban of deep exploitation was achieved in 2005 (Zhang et al., 2010; Shi et al., 2012). This series of practices altered the history of land subsidence in SWC. In Fig. S1, a summary of the groundwater pumping, groundwater level, and land subsidence in downtown Suzhou before, during and after the RGE was given (Shi et al., 2012). Here we consider 1997 as the beginning of RGE and summarize the milestones of the acts and outcomes (Fig. 1).

Multiple attempts have been made to monitor the ground deformation during the RGE, e.g., well observations, extensometers, and leveling (Chen et al., 2003; Shi et al., 2008a; Shi et al., 2008b; Wu et al., 2009; Zhang et al., 2010). Combined with the co-located hydrological observations, a qualitative correlation between groundwater level variation and aquifer deformation can be made at sparse locations (Wu et al., 2009; Shi et al., 2012). Generally, the groundwater level recovered from lowest values and land subsidence slowed after RGE (Huang and Zhou, 2011; Shi et al., 2012). However, the complex bedrock layout, heterogeneous substrata, and irregular pumping activities led to diverse surface responses at different locations (Zhang et al., 2007; Shi et al.,

2008b). Without quantitative in-situ measurements, the dynamic urban surface evolution cannot be determined. Consequently, a rigorous assessment of the RGE is difficult. Interferometric synthetic aperture radar (InSAR) provides deformation measurements in great spatiotemporal detail, i.e., a few to dozens of meters' spatial resolution, about biweekly sampling, and centimeter to millimeter precision in displacement measurements (Rucci et al., 2012; Crosetto et al., 2016; Hu et al., 2017). The benefits of this remote sensing tool have been clearly demonstrated in its broad applications, e.g., earthquakes (Bürgmann et al., 2006; Abir et al., 2015), glaciers (Mohr et al., 1998; Li et al., 2018), volcanos (Hooper et al., 2004; Shi et al., 2015), landslides (Cigna et al., 2013; Dong et al., 2017; Hu et al., 2019), reclamations (Xu et al., 2016; Shi et al., 2019), infrastructures (Ma et al., 2015; Wang et al., 2016; Qin et al., 2018), and nuclear explosion (Wang et al., 2018). InSAR has become a useful tool to reveal groundwater induced basin-wide surface and subsurface dynamics including hydrological properties (Hoffmann et al., 2003; Chen et al., 2016; Miller et al., 2017; Hu et al., 2018; Jiang et al., 2018; Zhou et al., 2018). Previous InSAR studies in Suzhou are limited by the incomplete and discontinuous observations, which are insufficient for a comprehensive assessment on the RGE policy (Gong et al., 2008; Zhang et al., 2011).

This paper presents decadal deformation measurements of Suzhou during the entire phase of the RGE. We use a hybrid small baseline subsets (SBAS), persistent scatterer (PS) interferometry (PSI), and distributed scatterer (DS) interferometry (DSI) to examine the spatial distribution of ground subsidence using multiple SAR sensors of ERS1/2, ENVISAT ASAR, and ALOS-1 during 1993–2010. We apply principal component analysis (PCA) to characterize the spatiotemporal properties of the inelastic compaction of confined aquifers and the deformation in shallower, unconfined soil layers. An inelastic compaction occurs when the effective stress exceeds the previous maximum value and causes irreversible compaction of aquifer system, whereas an elastic compaction is usually recoverable and is regulated by pore fluid pressure (Galloway et al., 1998; Haghghi and Motagh, 2019). To systematically quantify the surface response to the RGE, we analyze the decay

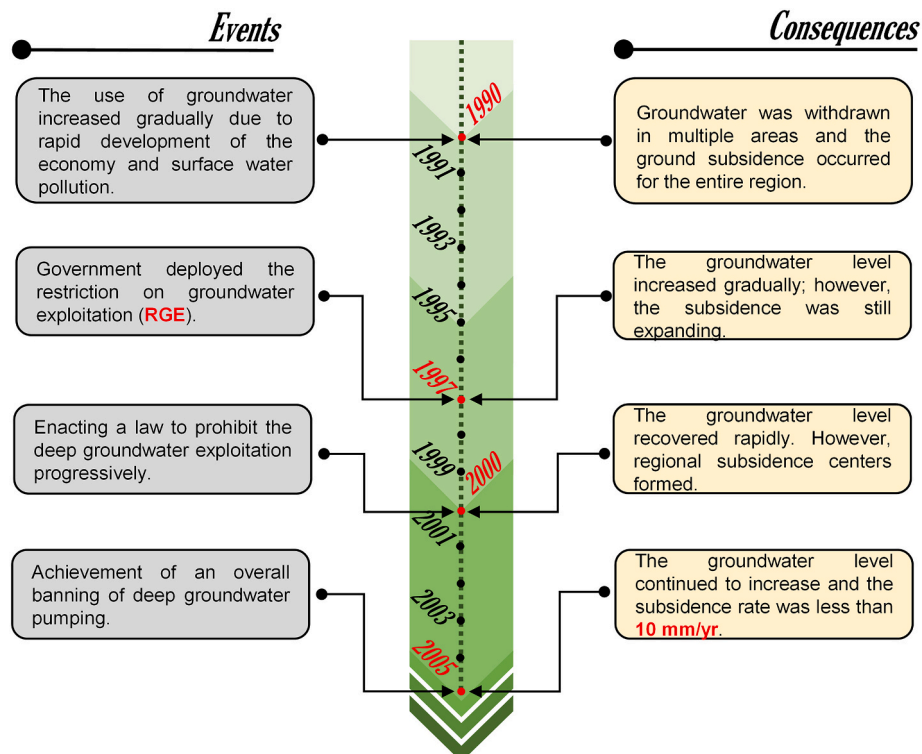


Fig. 1. Timeline of the development and control of land subsidence in the study area, modified from Shi et al., 2012.

properties of the long-term subsidence at selected locations. The different surface sensitivities help characterize the spatial impacts of the RGE. In addition, we infer the subsurface geological boundaries between shallow and deep aquifer layers (the sharp gradient in bedrock depth) from the decaying degree of subsidence. The mapped geological boundaries are important for civil construction, especially for underground developments. The InSAR-derived displacements reveal detailed urban surface subsidence in Suzhou during the RGE, enhancing our understanding of the roles of groundwater and subsurface features in subsidence development.

2. Materials and methods

2.1. Geological settings

Suzhou is located in the center of the YRD city group (Fig. 2) surrounded by four major lakes: the Taihu (T.H.) lake, Yangcheng (Y.C.) lake, Jinji (J.J.) lake, and Chenghu (C.H.) lake. The city is built above a river alluvial plain with an average elevation of less than 6 m above the sea level (Shi et al., 2007). The widely distributed Quaternary strata has an average depth of ~200 m, and it deepens from the west to the east (Fig. 2b) (Chen et al., 2003; Zhang et al., 2016). The abundant groundwater resource supported a long-term industrial growth in Suzhou when the original depth of groundwater level was ~2–3 m during the 1960s (Huang and Zhou, 2011). However, by the end of the 20th century, the city experienced drastic land subsidence due to continuous over-pumping, and the entire SWC region and Shanghai were facing the same problem (Zhang et al., 2003; Shi et al., 2008b). The bedrock topography in Suzhou was primarily formed during the Yanshan Movement at the end of the Mesozoic when intricate depressions and ridges were frequently formed (Yu et al., 2006). Therefore, the bedrock is undulating with large gradients (Figs. 2b-c), which has accommodated soil sediments in divergent thickness and complex substrata structures (Yuan and Zhou, 2001; Zhu et al., 2006). The cross sectional profile in Fig. 2c shows a heterogeneous geology in the substrata aquifer. The sediment thickness and stratigraphic complexity can contribute to

uneven surface subsidence when the groundwater was extracted from the substrata (Cigna et al., 2012). Fig. 3 presents a schematic view of the hydrogeological settings in Suzhou. The 2600-km² research area includes the Planned Area of Suzhou (PAS), of which the downtown is located between the J.J. lake and rock outcrops (Fig. 2a).

2.2. Data

a. SAR data sets

We collected SAR data sets from multiple spaceborne sensors including 38 descending scenes of ERS1/2 (2/1993–12/2003), 37 ascending (7/2003–10/2010) and 29 descending (3/2003–8/2010) scenes of ENVISAT ASAR, and 11 ascending scenes of ALOS-1 PALSAR-1 (2/2007–9/2008), image footprints in Fig. 2a.

b. Groundwater wells and bedrock depth

Monthly averaged groundwater levels from 17 wells (red triangles in Fig. 2a) were used for interpreting and analyzing the subsidence properties. The groundwater levels were measured at the main exploitation aquifer. We compiled the bedrock depth information from Shi et al., 2012 and Zhang et al., 2016 to jointly investigate and validate the inferred subsurface boundaries of sharp bedrock gradient.

c. Monthly precipitation and lake level

To demonstrate the potential temporal correlation between deformation and shallow water changes, monthly precipitation (mainly fall as rainfall) and the lake level (in the Wusong elevation datum) of T.H. lake were collected as a proxy for the variations in shallow water content (Townley and Trefry, 2000; Novakowski and Gillham, 1988). The rainfall records are from the annual report of Jiangsu Province (Bureau of Statistics, Jiangsu Province), and the lake level records are from the annual report on water regime in Taihu Basin (Taihu Basin Authority, Ministry of Water Resources, China).

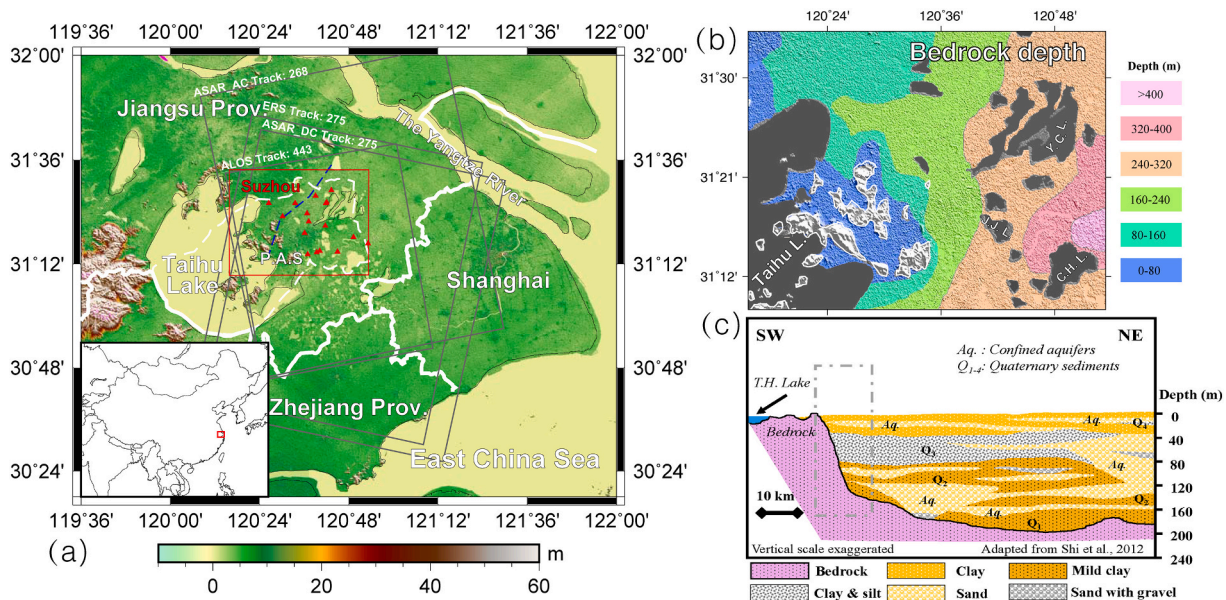


Fig. 2. Study area of the Suzhou city in the Yangtze River Delta. (a) The elevation (meters above the sea level) and SAR data footprints. The red box indicates the area of Suzhou; the thick solid white lines indicate the provincial administration boundary and the dashed white line is the Planned Area of Suzhou (PAS); the red triangles show the well locations; the satellite footprints of ERS descending track 275, ASAR ascending track 268, ASAR descending track 275, and ALOS-1 ascending track 443 are marked by grey boxes. (b) Contour map of the depth to the bedrock (Quaternary sediment thickness) modified from Zhang et al., 2016. The depth becomes larger from the west to the east, with a sharp gradient close to the group of bedrock outcrops (white polygons); (c) A hydrogeologic cross sectional profile (blue dashed line in panel (a)), modified from Shi et al., 2012. The dashed grey box indicates a sharp gradient in bedrock depth to the west of downtown. (For interpretation of the references to colour in this figure legend, the reader is referred to the web version of this article.)

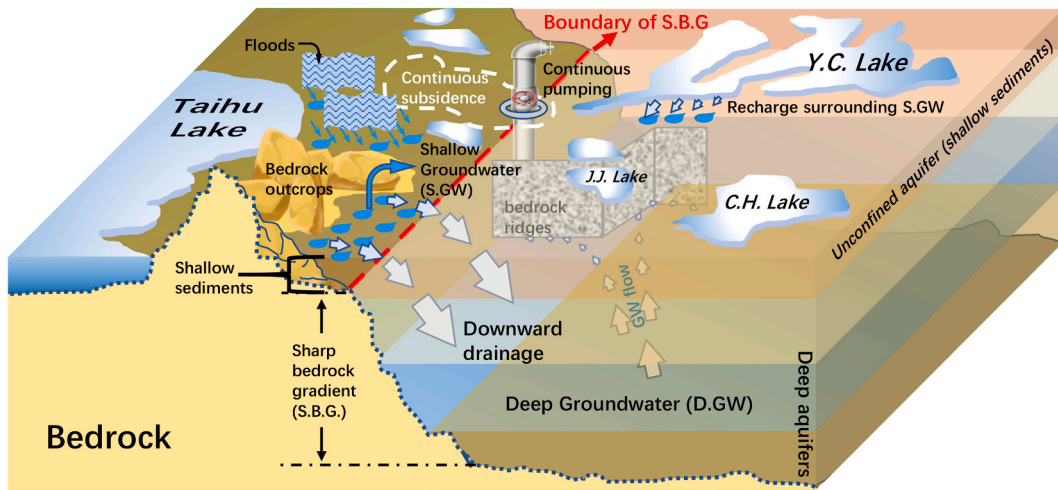


Fig. 3. Schematic view of hydrogeological elements in Suzhou. Y.C. Lake: Yangcheng Lake, J.J. Lake: Jinji Lake, C.H. Lake: Chenghu Lake.

2.3. Methods

a. Multitemporal InSAR

We use SBAS (Berardino et al., 2002) and integration of PS and DS interferometry (Ferretti et al., 2011) to estimate the surface deformation. The widely distributed vegetation, rapid urbanization, and drastic subsidence have contributed to serious decorrelation in ERS interferograms. The SBAS technique can effectively improve phase coherence by grouping optimal subsets of coherent interferograms, which also works for small SAR datasets (Samsonov, 2010). To best incorporate coherent

interferograms, SBAS was adopted to both ERS and ALOS data. The later time period of ASAR (2003–2010) exhibits good coherence in the urban area and shows a reduced subsidence. The PS method was used for the ASAR data, given plenty of phase stable targets, i.e., persistent scatterers, are available in the research region. To improve the measurement coverage and density, we integrated the PS results with DS extensions by including moderate coherence ground targets (Shi et al., 2019). Fig. 4 shows the baseline information of the four datasets.

The doppler instability caused by the later failed gyro on the ERS2 platform in early 2000 discontinued the coherent SAR pairs afterwards (Miranda et al., 2005; Meadows et al., 2005; Gong et al., 2008). A careful

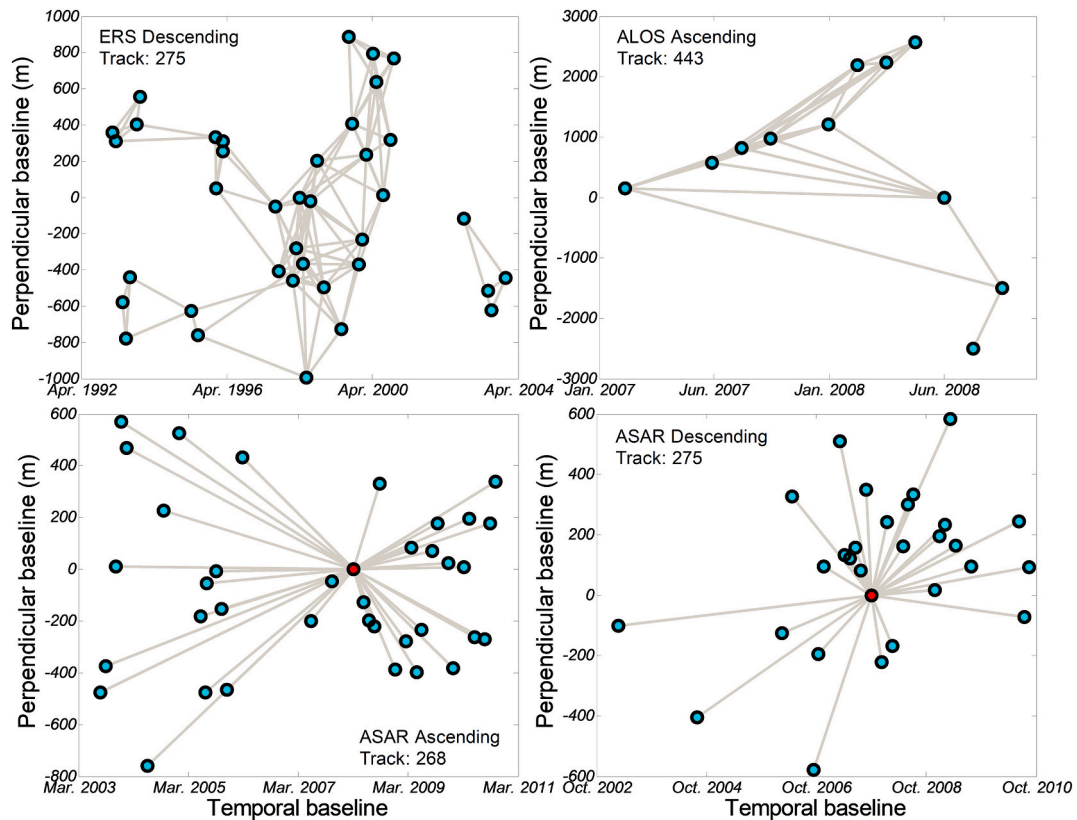


Fig. 4. Baseline information for ERS1/2, ALOS-1 and ENVISAT ASAR datasets. The circles indicate SAR acquisitions and the lines show the image pairs. The red dots represent the master images selected for the time series analysis. (For interpretation of the references to colour in this figure legend, the reader is referred to the web version of this article.)

manual selection of the interferograms is necessary to exclude the very low coherence pairs in the ERS dataset. The spatiotemporal baseline thresholds for ALOS-1 interferogram were 1800 m and 1.7 years, respectively. We applied multi-looks of 2×10 and 5×10 to the range and azimuth directions for ERS and ALOS data, respectively. The SBAS exploits singular value decomposition (SVD) method to estimate the deformation components from the unwrapped phase (Casu et al., 2006). For the PS and DS processing of ASAR datasets, interferograms were generated using 1×5 multi-look in the range and azimuth directions. The integration of PS and DS was completed using a two-tier network, i. e., the PS reference network and the DS extension (Shi et al., 2018). Specifically, initial PS candidates were selected using an amplitude dispersion index (ADI) smaller than 0.4 (Ferretti et al., 2001). Solutions of PS arcs with the normalized temporal coherence higher than 0.7 remain as qualified candidates for the first-tier reference network (Ma and Lin, 2016; Shi et al., 2018). The DS extension was completed using local star networks that link DS candidates to their nearest PS reference point. DS arc parameters are estimated from phase values of refined interferograms after homogeneous filtering (Ferretti et al., 2011). In our case, we kept DS arc solutions with the normalized temporal coherence higher than 0.68.

b. Time series decomposition from PCA

The PCA method can reduce the effective number of dimensions in a data set while preserving its features (Lischeid, 2009). Depending on the characteristics of data matrix, there are six modes of PCA (Richman, 1986). In particular, T-mode (TPCA), with data matrix of locations versus time, is often used in GPS analysis, electronic distance measurements, and time-series InSAR analysis, etc. (Lin et al., 2010; Ji and Herring, 2011; Rudolph et al., 2013; Chaussard et al., 2014a). We use the TPCA to retrieve different deformation sources of the aquifer from long-term InSAR observations. The data matrix is organized as $m \times n$, populated by the displacement values of the m ground locations (pixels) considered at each of their n time steps (acquisitions). PCA transformation was realized using an SVD of the data matrix (Gerbrands, 1981),

$$\begin{cases} P = XW \\ X = U\Sigma W^T \end{cases} \quad (1)$$

where P is the $m \times n$ score matrix of the principal components (PCs), X is the $m \times n$ data matrix created using the ERS and ASAR datasets ($n=104$), U is an $m \times m$ matrix containing the left singular vectors of X , Σ is an $m \times n$ rectangular diagonal matrix containing the singular values of X , and W is an $n \times n$ matrix containing the right singular vectors of X , i.e., the eigenvectors of the data covariance $X^T X$, where T indicates the transpose. The score maps from P and the eigenvectors from W describe the spatial and temporal characteristics of the measured deformation, respectively (Chaussard et al., 2014a). To determine the dimensions that best describe the deformation data, we tested the stability of the obtained PCs using a risk function based on the resampling methods of bootstrap and jackknife (Text S1) (Besse, 1992). According to Fig. S2, both of the risk estimates suggest the stability of the first four-dimensional subspaces (Besse and de Falguerolles, 1993). We retained the first four PCs, while the subsequent components are negligible and likely represent atmospheric contributions and other noise terms (Fig. S3) (Chaussard et al., 2014a; Cohen-Waeber et al., 2018).

c. Decay coefficients and time response

Aquifer deformations in Suzhou are likely evolved in space and time due to the artificial (e.g., spatiotemporal irregular pumping activities) and natural (e.g., heterogeneous hydrostratigraphic units) disturbances (Shi et al., 2007; Shi et al., 2012; Zhang et al., 2010). Generally, the variation of groundwater levels will not immediately deform the

sedimentary layers due to the delayed equilibration of hydraulic pressure among the aquifers (Hoffmann et al., 2003; Bell et al., 2008). This time delay is complicated by various aquifer layers of different hydraulic diffusivity. By relating the vertical deformation to the change of effective stress (first-order approximation of the hydraulic head), the estimation of time lag requires continuous records of the layered deformation and groundwater level in this nonlinear system (Hoffmann et al., 2003; Bell et al., 2008; Miller et al., 2017). Given the difficulties in acquiring satisfactory data and the complicated computation of the modeling, we use the time lag between the InSAR-derived regional subsidence slowdown and the beginning of RGE to evaluate the impacts of the RGE. Only InSAR time series are required and the time responses can be calculated from actual displacement measurements instead of model interpolation. Deformation of aquifer layers can be characterized by modeling the vertical movements as an exponential function of time (Terzaghi, 1925; Chaussard et al., 2014a; Hu et al., 2018), such that:

$$def(t) = M(e^{\mu t} - 1) \quad (2)$$

where $def(t)$ is the time-series vertical deformation, M is the magnitude coefficient characterizes the cumulative deformation, and $\mu \in [-1, 0]$ is the decay coefficient. In Section 3.2, we compare the decay coefficients during two periods to reveal the spatially variant recovering processes during the RGE. The time response t_{res} approximates the time required by the ground surface to reach a relative stable and reasonable subsidence since the implementation of the RGE, i.e.,

$$t_{res} = \frac{\ln\left(\frac{\sigma|\bar{v}|}{M\mu^2}\right)}{|\mu|} \quad (3)$$

where σ is a scaler and $|\bar{v}|$ is the mean velocity of the time-series deformation. The time response t_{res} corresponds to the situation when the second derivative of the cumulative subsidence (Eq. (2)) equals to a scaled velocity $\sigma|\bar{v}|$. Such that, the time response of the ground surface to the RGE can be quantified and differentiated among the targets. A reasonable σ depends on a *prior* knowledge of the geodetic and hydrological records. According to Wu et al., 2008 and Shi et al., 2012, the subsidence was believed to be under control when the average rate was smaller than 10 mm/yr (5 mm/yr for some areas) in the fastest subsiding downtown, which was approximately 5%–10% of the rate before the RGE (Huang and Zhou, 2011; Shi et al., 2012) and we used σ as 5% in this study.

3. Results

3.1. Deep and shallow aquifer deformation from PCA

The large, dominant deformation can account for the majority of data variance in a PCA, whereas the remaining small components still explain meaningful deformation sources (Cohen-Waeber et al., 2018). Scree plot of the data variance explained by the PCs was given in Fig. S2. Figs. 5a-d show the spatial responses of the first four PCs with their temporal behaviors in Figs. 5e-f. The first component corresponds to the major trend of subsidence at meter-level magnitude. In Suzhou, the groundwater level was lower than the historical lowest (the pre-consolidation water head) before the exploitation ban. The deformation of aquifers was mainly elasto-plastic and even visco-elasto-plastic (Shi et al., 2012). Fig. 5e highlights a strong inelastic compaction in the early stage of the PC1 eigenvector, whereas the contribution from the RGE in slowing down the settlement can be observed after 2003. Average subsidence rate after 2003 yields only about a quarter of that before 2003. Behind the significant reduction of land subsidence was the rapid recovery of deep groundwater level. Fig. 6 presents the interpolated groundwater level at winter time using monthly averaged well records based on the Kriging method (Lophaven et al., 2002). The tool for spatial interpolation is available at <http://www.omicron.dk/dace.html>. The

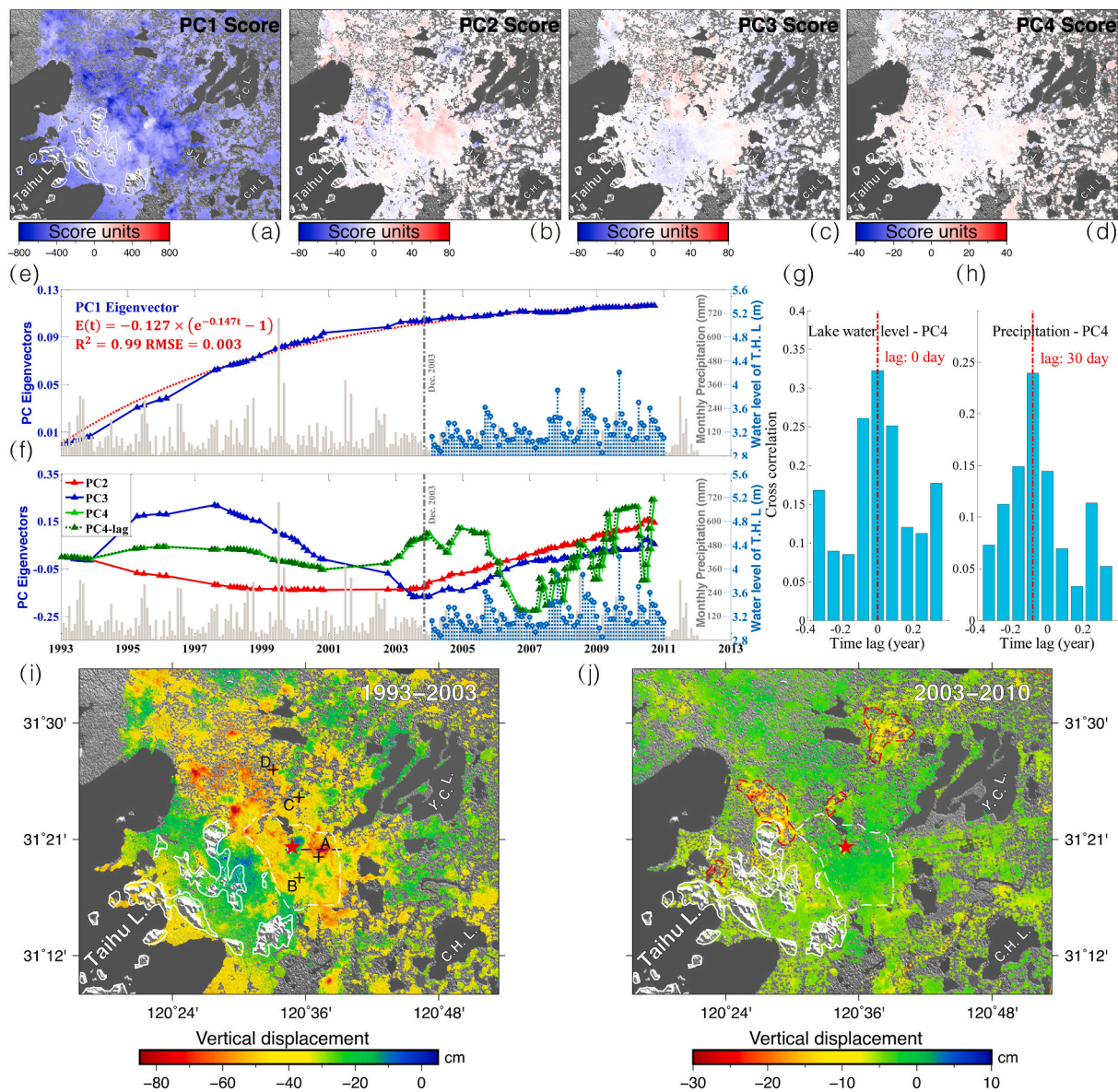


Fig. 5. PCA characterization of the vertical surface displacements. (a)-(d) Score maps of components PC1 to PC4. (e) Eigenvector of PC1 with the red dashed line fitted by the exponential decaying function; (f) Eigenvectors of PC2 to PC4, along with the one-month delayed PC4. (g)-(h) Cross correlation between the lake level and PC4, the precipitation and PC4, respectively. (i)-(j) Cumulative deformation maps during 1993–2003 and 2003–2010. The downtown Suzhou refers to the former Canglang, Pingjiang, and Jinchang districts (now merged into Gusu district), indicated by the white dashed polygon. The blue dashed line in panel (i) indicates the cumulative deformation profile in Fig. 7c and the black crosses with annotations show the locations of field photos in Fig. 8. The red dashed polygons in panel (j) are areas detected with evident continuous subsidence. The red star shows the deformation reference on the stable Huqiu bedrock. The score maps can be converted to deformation (in cm) by multiplying the corresponding eigenvectors at the given time. (For interpretation of the references to colour in this figure legend, the reader is referred to the web version of this article.)

remarkable subsidence slowdown along with the groundwater recovery was given at locations W2 and W3 in Figs. 7a-b. We estimated an overall decay coefficient of about -0.147 for the inelastic subsidence in Suzhou, as suggested by PC1 eigenvector. Spatial distribution of the inelastic compaction is clearly outlined by the score map in a southeast-northwest direction (Fig. 5a), consistent with the groundwater level depressions in Fig. 6. Note that the magnitude of cumulative subsidence is correlated with the thickness of underlay sediments (Fig. 7c). A comparison between the pre- and post-2003 urban subsidence was given in Figs. 5i-j.

The widespread and dramatic inelastic subsidence caused considerable elevation loss in Suzhou, which damaged the road systems and threatened safety of transportation during flooding. Therefore, the government began to renovate the main stems by elevating the original road surfaces (e.g., Figs. 8a-b). The new road surfaces were elevated by

~ 0.5 m. The roads were elevated not only in downtown but also in the countryside where needed. Site D in Fig. 5i is a village surrounded by riverways. In the 1970s, the villagers used ropes of 1–2 m to fetch water from the river, as the river surface and the ground was about 1.7 m difference in height. Anecdotal evidence suggests that the village experienced the most rapid subsidence in the 1980s and 1990s. Fig. 8d shows that the water surfaces in the present day almost reach the foundations of the houses besides the river. More remarkably, the elevated road surface on the other side of the house is now leveling to or even burying the old windowsill. However, not all sinking roads can be elevated in high priority and at a reasonable cost. In some lower altitude areas such as >300 fishponds in site C, the sinking ponds were connected entirely due to the reduced elevation of land surfaces between them, and eventually transformed into a wetland park (Fig. 8c).

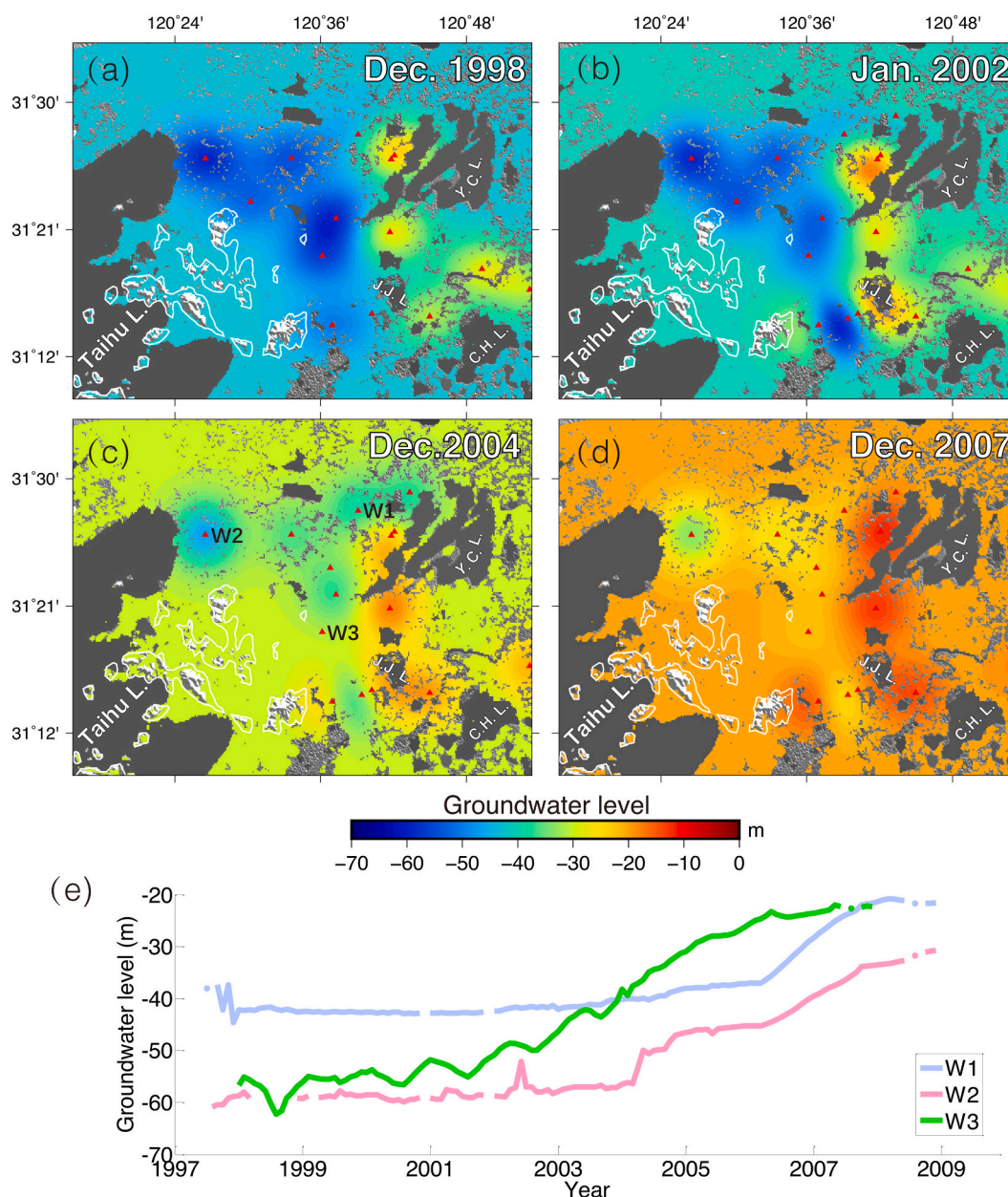


Fig. 6. Interpolated groundwater level in (a) 12/1998, (b) 1/2002, (c) 12/2004, and (d) 12/2007. The red triangles indicate wells that are available for interpolation. (e) The time-series groundwater level in wells W1, W2, and W3. A delayed recovery of water level has been observed in wells W1 and W2, corresponding to the continuous subsiding sites in Fig. 5j. (For interpretation of the references to colour in this figure legend, the reader is referred to the web version of this article.)

The PC2 score map shows distinguishable patterns with negative values (blue colour) in the satellite counties around Suzhou downtown (Fig. 5b). Combined with its eigenvector, PC2 suggests that considerable land subsidence continued after 2003 over these bluish areas, whereas the remaining parts with non-negative score values present an evident slowing down. The continuous subsidence was monitored in a later time period 2003–2010 in Fig. 5j. Such behavior of PC2 can be related to the uneven groundwater recovery within the deep, confined aquifers, as we observe the locations of continuous subsiding were in good agreement with the groundwater depressions that lasted through the later time period (e.g., on sites W1 and W2 in Fig. 6c). Although, deep groundwater wells were largely sealed by the government during RGE, some were still active for production especially out of the downtown Suzhou. Our field investigation has confirmed that these locations are industrial sites with manufactures such as printing, papermaking, and metalwork, which consume abundant water. The time series records in W1 and W2

suggest that the continuous pumping activities led to a delayed but stronger rebound in their water levels probably due to a decreased or ceased withdrawal (Fig. 6e). Except these surrounding counties, PC2 shows no evident subsiding continued in downtown. According to the deformation maps in Figs. 5i–j and the well records, it seems that PC1 and PC2 capture the subsidence sources related to the deep groundwater variations. That is, the dominant inelastic compaction by the prolonged low groundwater level (PC1) and the formation of continuous subsidence by the spatially uneven deep groundwater recovery (PC2).

Different to the first two components, PC3 and PC4 may represent the deformation related to the shallow unconfined sediments. The PC3 score map (Fig. 5c) highlights the difference between the shallow sediments around bedrock outcrops (blue colour) and the deep aquifers (white/red colour). The eigenvector of PC3 indicates a strong decay of subsidence and even rebound for the blue patches in the period of 1998–2003 while they continued to subside later during 2003–2010.

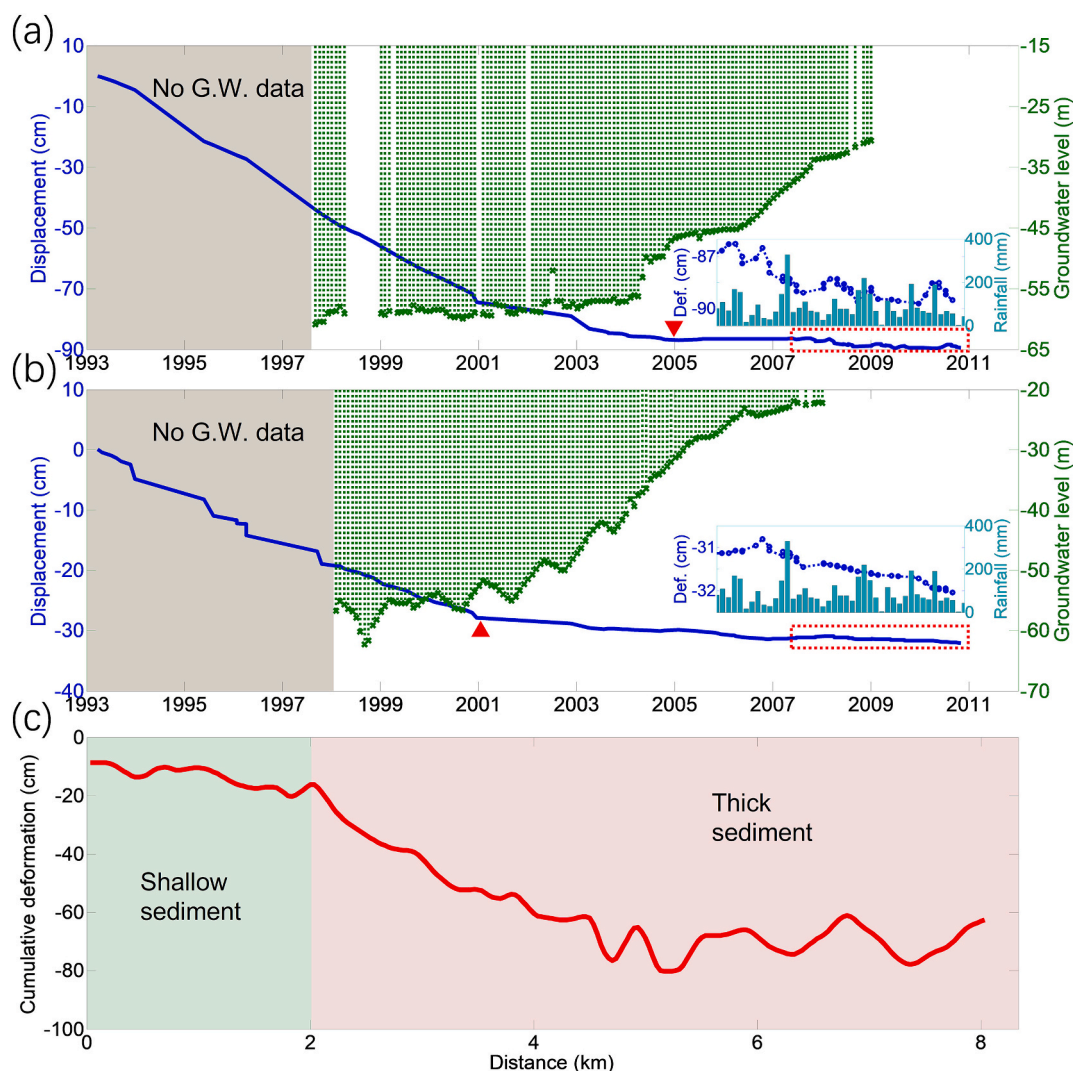


Fig. 7. Land subsidence on selected locations. Subsidence time-series along with the monthly groundwater level at location (a) W2 and (b) W3 (Fig. 6c), red rectangle indicates slowdown in the subsidence, the inset shows the amplified view of the red dashed box with the monthly rainfall. (c) Profile of cumulative subsidence along the blue dashed line in Fig. 5i, crossing the shallow (Huqiu mountain area) and the thick sediments. (For interpretation of the references to colour in this figure legend, the reader is referred to the web version of this article.)

Similar responses were also found around water bodies (e.g., Y.C. lake, J.J. lake). This deformation source is probably due to the recharge and discharge of shallow unconfined/semi-confined groundwater (e.g., the 1998 Yangtze River Basin flood and the 1999 Taihu Basin flood), which will be discussed in Section 3.2. PC4 is the only component that captures a seasonal variation in the later period 2006–2010, thanks to the more frequent SAR sampling and the significantly reduced subsidence magnitude. The periodic deformation is probably due to the poro-elastic effect induced by the variations of water content in the unconfined sediments, which is sensitive in shallow depth (~ 2 m) (Chen and Hu, 2004). We analyzed the correlation between the PC4 eigenvector (after 2006), the monthly precipitations, and the monthly lake level of T.H. (Figs. 5g–h). The lakes in Suzhou are shallow (~ 2 m), e.g., the average depth of T.H. lake is 1.81 m (max. 2.6 m). Consequently, these water bodies reflect the water content in the nearby shallow soil layers, especially within the ~ 2 -m sediments. The cross-correlation in Fig. 5g suggests that the deformation has an immediate response to the changes of lake level without phase delay. However, time delay often exists between the sediment deformation and precipitations due to infiltration (Calabro et al., 2010; Ardizzone et al., 2011; Cohen-Waeber et al., 2018). Within the limit of SAR temporal resolution, we found about one-month time lag between the precipitation and the displacement response

(Fig. 5h). However, neither rainfall nor SAR data is daily sampled so the cross-correlation results may be biased. Another factor that might be related to PC4 is the thermal effect of buildings, given that the measurements were from an urban environment. Studies have revealed thermal coefficients of only ~ 1 mm/ $^{\circ}$ C for buildings of 100-m height (Ma et al., 2015; Zhou et al., 2019). However, considering the average building height in Suzhou is about ten meters (Fig. S4), the contribution from thermal effect, if there is, would be small to PC4. Details on the cross-correlation between PC4 and temperature can be found in the supplementary material.

3.2. Spatial variant decaying subsidence

To evaluate the evolution of the decelerated deformation, the decay coefficient μ was calculated separately for an earlier period of 1993–2003 and the entire period of 1993–2010, using $400 \text{ m} \times 400 \text{ m}$ ground patches. Fig. 9 shows the spatial patterns of μ , where smaller values represent a faster decaying and larger values (close to 0) indicate slower decaying and even a quasi-linear trend. The difference in μ suggests the spatial variant effects of RGE. Fig. 10 gives a differential map by subtracting μ of the entire period from that of the earlier period, and highlights the regions with positive change (red dashed polygon),



Fig. 8. Field photos of the ground subsidence in Suzhou. (a)-(b) Sites A and B. The elevated road surface based on the sinking ground (old road surfaces). The land surface of the shop entrances used to be the same to that of the original road surfaces. (c) Site C. The wetland park consisted of over 300 individual but connected fish ponds. (d) Site D. The sinking village along the riverside, where the house foundations are almost leveling to the shoreline (the white dashed line) and the old windowsill of the house is now buried by the new elevated road surface. The ground surface used to be ~1.7 m above the river in the 1970s. The locations of the field photos are marked by black crosses in Fig. 5i.

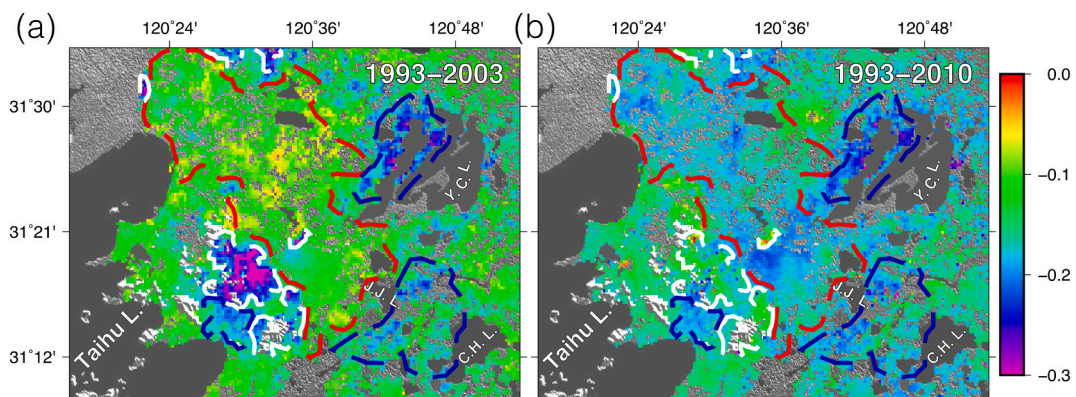


Fig. 9. Decay coefficients μ during (a) 1993–2003 and (b) 1993–2010. The dashed polygons are the selected regions with specific μ value changes that are further discussed in Fig. 10a.

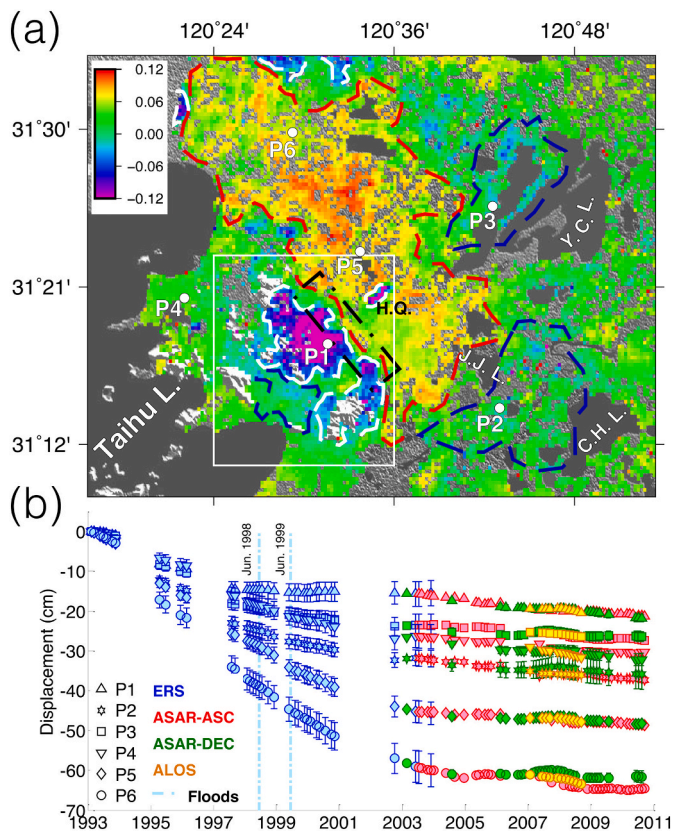


Fig. 10. The spatiotemporal patterns of decaying subsidence. (a) Differential μ between the earlier period 1993–2003 and the entire period 1993–2010. The red, white, and blue dashed polygons show selected zones with positive, negative, and stable μ changes. The black dashed rectangle indicates a region with sharp gradient in bedrock depth, illustrated in Fig. 2c. (b) Time-series displacements of 6 targets: P1 (shallow sediment with negative change of μ), P2–3 (unchanged μ with significant decay near water bodies), P4 (unchanged μ with minor decay), and P5–6 (the main subsiding region with positive change of μ). (For interpretation of the references to colour in this figure legend, the reader is referred to the web version of this article.)

negative change (white dashed polygons), and nearly unchanged with considerable decaying (blue dashed polygons).

a. The positive change zone (PCZ) of decay coefficients

By comparing with the deformation (Fig. 5i) and the groundwater level (Fig. 6), PCZ coincides with the main pumping area where the groundwater level in 1998 was as deep as ~ 60 m. It extends from the southeastern downtown to the northwest of the imaged area (the red dashed polygon in Fig. 10a). According to Fig. 2b, the bedrock depth in PCZ is between 160 and 240 m. The thick aquifer layers compacted continuously during the 1990s, contrasting to a strong decay in the 2000s due to the rapid recovery of the deep groundwater (Fig. 7). Representative land subsidence in PCZ was given at P5 and P6 (Fig. 10b). The cumulative settlement at P6 is ~ 0.6 m during 1993–2003 but < 0.1 m during 2003–2010. The strong decaying generated by the RGE in PCZ resulted in an obvious exponential change in μ from about -0.1 (Fig. 9a) to -0.2 (Fig. 9b).

b. The negative change zone (NCZ) of decay coefficients

Negative changes in μ concentrate in areas with shallow sediments around the bedrock outcrops (the white dashed polygons in Fig. 10). Different from the thick aquifers in the PCZ, settlement of the thinner sediments would be small and mainly regulated by shallow unconfined/

semi-confined groundwater variations (Shi et al., 2007; Wu et al., 2009). The average subsidence rate in the NCZ was of ~ 10 mm/yr. Target P1 represents the time-series deformation of the NCZ (Fig. 10b), showing a strong decay started around 1998 which was not observed in other targets (P2–P6). The earlier decaying may be related to the two flood events in the Taihu basin (blue vertical lines in Fig. 10b). In 1998, the Yangtze River Basin flood lasted from mid-June to early-September (Zong and Chen, 2000) due to the two extraordinary wet seasons (Liu et al., 2008; Yan, 1998). The flood impacted many provinces, including Jiangsu and Zhejiang where the T.H. lake basin lies (Lyu et al., 2018). One year later in June 1999, another catastrophic and regional flood struck the T.H. lake basin (Li et al., 2013) due to the heaviest contemporary rain since 1928. The flood raised the T.H. lake level to 5.08 m a.s.l., 0.29 m higher than the prehistoric peak (4.79 m) recorded during the 1991 flood (Wu, 2000).

Two floods in consecutive years caused serious waterlogging in the low altitude areas of Suzhou. The shallower, unconfined aquifer was saturated and covered by the surface water, leading to strong decay in sediment compaction and even slight rebound immediately after the flood (Jun. 1998 to Jun. 1999) revealed by P1. In a short time period, the surficial water can hardly reach the deep aquifers before run-off. Groundwater records in the main pumping layer showed no evident rise during and after the floods (Fig. 6e). The hydraulic potential between the deep aquifers and the NCZ still existed which would cause further intrusion of shallow water downdeep to the adjacent aquifers. In addition, the steep slope of the bedrock (Fig. 2c) had essentially promoted the downward draining, as illustrated in Fig. 3. When the redundant shallow water drained away, the water level of the unconfined layer in NCZ declined accordingly, causing reduction in water pore pressure, and thus, continued subsidence of the land surface (later period of the P1 time series).

c. The unchanged zone (UCZ) of decay coefficients

The blue dashed polygons highlight regions with significant decay effects throughout the entire period, referred to as the UCZ-S. The lower and stable μ value suggests that 1) the recovery of groundwater was faster than that in the PCZ, and 2) the decaying process appeared more uniform over time regardless of the act of the RGE. UCZ-S locates mainly around the water bodies, e.g., the west of the Y.C. lake, the area between the C.H. lake and the J.J. lake, and the southeastern edge of the T.H. lake. These lakes became an ideal source to continuously discharge to the surrounding aquifers. Buffer zones at the lakeside had relatively higher groundwater levels during 1998 and 2007 (Fig. 6). Therefore, the subsidence decay arrived earlier in the UCZ-S than in the PCZ. However, not all areas around the lake were subject to a significant decay. For example, lower μ was found around the southeastern edge of the T.H. lake but not to its northeast. This is probably due to the heterogeneous substrata units, bedrock topography, and continuous pumping, etc. Representative subsidence time series of UCZ-S were given at P2 (between J.J. lake and C.H. lake) and P3 (Y.C. lake) where μ is about -0.2 .

Green patches without assigned polygons are areas where subsidence follows a minor decay trend ($\mu = \sim -0.1$), referred as UCZ-M. The subsidence process in the UCZ-M (P4) was not slowed down as effectively as that in the UCZ-S. Such that, under an equivalent magnitude of subsidence (e.g., P3 and P4), a slower decay in the UCZ-M suggests that a longer time is warranted for a recovery from the continuous land sinking (discussed in Section 4.2).

4. Discussion

4.1. Subsurface boundaries of sharp gradient in bedrock depth

The contour line and cross sectional profile (Figs. 2b–c) confirm the existence of the sharp gradient bedrock (S.G.B) that separates the shallow and thick sediments (Fig. 3). According to the above decay

property, the NCZ zones were identified as shallow sediments and the colour contrast of patches in the dashed black rectangle (Fig. 10a) was due to the distinct deformation behaviors over the divergent sediment thickness. In other words, the discontinuity of colour tone in the differential μ map can essentially indicate the dividing line of bedrock depth. We inferred the potential boundaries of S.G.B by tracking the blue-purple patches. Fig. 11 shows the enlarged map of the boxed area in Fig. 10, superimposed by the contour lines of 40- and 80-m depth (white dashed lines) to bedrock (adapted from Zhang et al., 2016). The inferred boundaries are marked in colour lines. In particular, the blue sections indicate an overlap (consistency) between the inferred boundaries of S. G.B and the known contour lines. The red sections are updated (newly identified) boundaries with respect to the old knowledge. The red dashed lines indicate undetermined boundaries because of data discontinuity due to InSAR decorrelation over vegetated areas. For example, the boundary discontinuity in box A spans across the densely forested mountainous area where InSAR data is missing (Fig. 11b).

A stronger colour contrast implies a steeper bedrock gradient such as the black dashed rectangle in Fig. 10a and around the Huqiu outcrop (H. Q. in Figs. 10&11). Fig. 11b projects the inferred boundaries in the boxed areas to an aerial imagery from Google Earth (source: WorldView-2). In this built area, we conclude a much thicker soil layer (~160 to 240 m) on the right side of the colored lines, whereas perhaps only tens of meters' depth on the left side. Apart from distinguishing the spatially divergent sediments in these densely built regions, the boundary helps enhance our understanding of underground structure and flow dynamics in the city. More important, the determination of shallow bedrock distribution is valuable for urban planning, especially for the construction of underground transportation and foundation piling. In addition to those highlighted patches (Fig. 11a), suspicious regions with a similar characteristic were also detected (the white dashed polygons in Fig. 10a).

4.2. Surface time response to RGE

Substrata heterogeneity, initial water level, and an uneven execution of the RGE contributed to the diverse surface response. Unsynchronized groundwater recovery was observed by well records (Fig. 6), and thus unsynchronized subsidence slowdown (Figs. 7a-b). The depth to the groundwater level at W1 stayed about 40 m until a sudden rebound in 2006 and similarly an abrupt rise at W2 until 2004 (Fig. 6e). On the contrary, the groundwater level at the downtown (W3) rose immediately in a more steady way than the northern area since the start of the RGE, although the initial water levels in W2 and W3 were almost equivalent in 1998. The slower recovery of deep groundwater is the principal reason for the continuous subsidence in the northern suburbs (Fig. 5j). Since the complicated process of groundwater recovery was eventually reflected in aquifer deformation, the surface time response provides direct evidence to evaluate the RGE's regional impact. Based on Eq. (3), we calculate t_{res} using the mean InSAR measurements in an arrangement of blocks and each block is 1.12×1.35 km. Note that blocks with the average subsidence rate of smaller than 10 mm/yr were masked out as the 5% criterium of σ would lose its practice in stable and less deforming areas. Fig. 12 shows the estimated time response in years since the start of RGE in 1997, i.e., $t_{res} = 1$ means the start of 1998, and captures the first-order approximation on how fast the urban surface reacted to the restriction policy.

An elongated corridor (green dashed polygon) connecting the southeastern edge of the T.H. lake and the Y.C. lake was highlighted by the shortest time response of ~9.5 years (blue patches in Fig. 12). The corridor covers most of the downtown area. The immediate water level recovery in collocated well W3 implies a timely stop of pumping after the RGE. Consequently, the effect from RGE came earlier in downtown than the surroundings. Our estimates indicate that land subsidence in the downtown (although with a large magnitude) was expected to be well controlled after 2005 (rate declined to 11 mm/yr with a deceleration smaller than 2 mm/yr^2 at the fastest subsiding zone around site A in

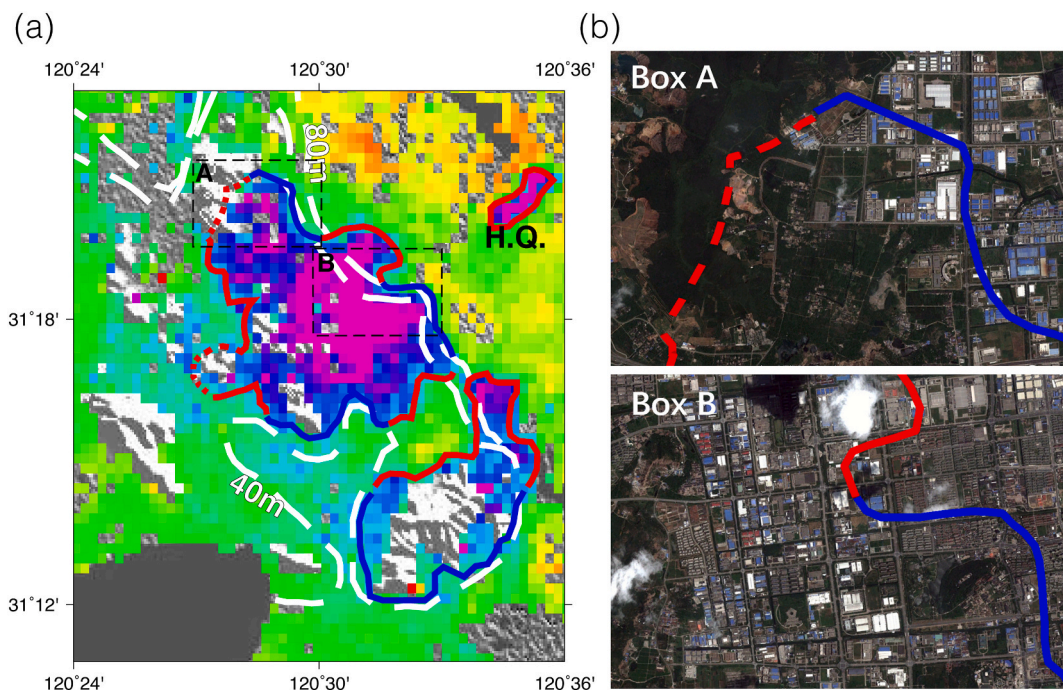


Fig. 11. Boundaries of shallow sediments. (a) Enlarged view of the white box in Fig. 10. Blue and red lines show the inferred S.G.B boundaries. White lines show 40- and 80-m depth contour, modified from Zhang et al., 2016. The blue lines confirm the known contour lines and the red lines indicate the potential and updated boundaries that are newly discovered. The red dashed lines are undetermined due to InSAR decorrelation. (b) Optical imagery from Google Earth (source: WorldView-2) on the areas outlined by the dashed black boxes in panel (a). The thickness of underlying sediments is supposed to be quite different at two sides of the colored lines. (For interpretation of the references to colour in this figure legend, the reader is referred to the web version of this article.)

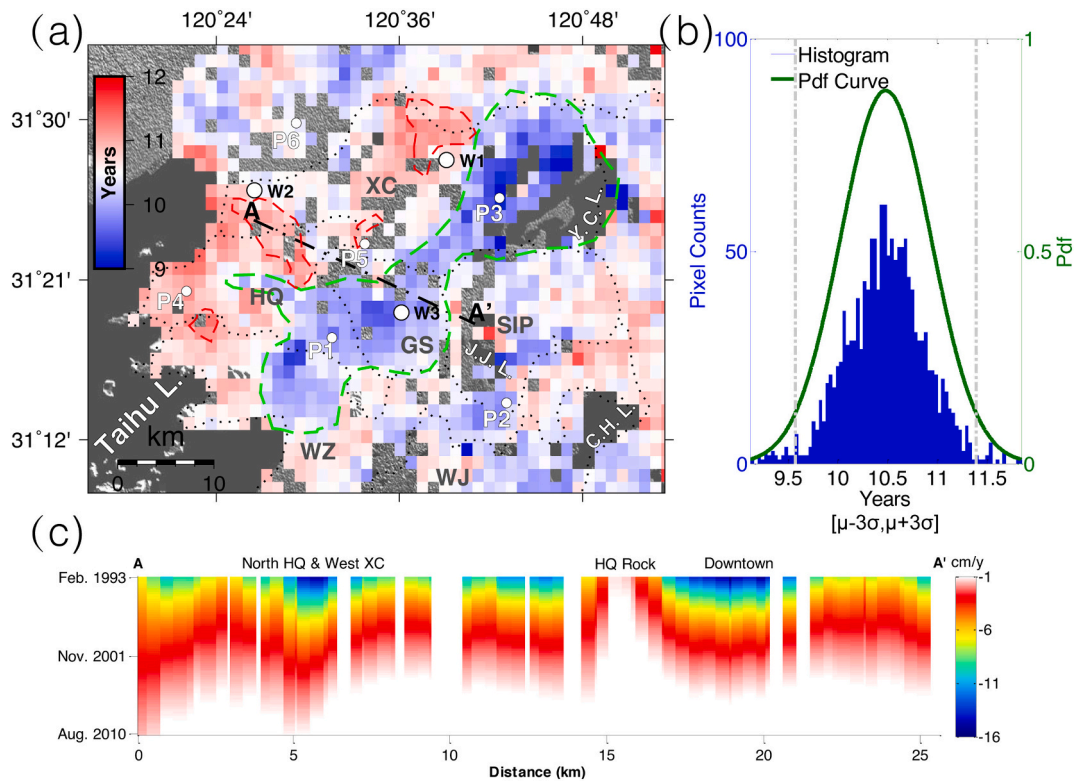


Fig. 12. Estimation of the time response to RGE. (a) Map of the estimated time response (years since the start of 1997). The dotted black line indicates administrative district boundaries of Gu-Su District (GS), Hu-Qiu District (HQ), Xiang-Cheng District (XC), China-Singapore Suzhou Industrial Park (SIP), Wu-Zhong District (WZ) and Wu-Jiang District (WJ). The green dashed line indicates the corridor with the fastest time response. The red dashed lines indicate continuous subsidence areas in Fig. 5j. (b) Histogram and PDF (probability density function) curve of the time response estimates. (c) Profile of the time varying velocity along AA' in panel (a). The statistics suggest an overall time response of 10.5 ± 0.9 years (95% confidence level) to the implementation of RGE. (For interpretation of the references to colour in this figure legend, the reader is referred to the web version of this article.)

Fig. 5i). This finding agrees with the in-situ measurements (Zhang et al., 2010; Huang and Zhou, 2011; Shi et al., 2012). Short time response was also observed near J.J. and C.H. lakes, where groundwater level remained at a higher level since Dec. 1998 and the subsidence is small and less affected by the over-pumping activities (Figs. 6a-d). Once the RGE took effect, the closer the distance to water bodies, the sooner the groundwater would be recovered and the ground subsidence would slow down (e.g., P2 and P3).

A lengthy time response was mainly located to the north of the downtown (XC district, HQ district, western WZ district) and eastern SIP. Especially, red patches were concentrated to the north of the blue corridor, where approximately 11.5 years were expected for those areas to recover from the compaction. Note that all the continuous subsidence (red dashed polygons in Fig. 12a) is located to the north side of the corridor. On the one hand, spatially irregular pumping activities led to the distinct patterns of the corridor and the northern red patches. The continuous pumping (e.g., W1, W2) prevented the deep groundwater from recovering as expected, resulting in the lagged surface response. On the other hand, the bedrock, e.g., the Huqiu outcrops and those subsurface ridges (e.g., Johnson et al., 1977), could act as a natural barrier that stops the substrata groundwater flow (Fig. 3). Consequently, an overall balance of groundwater in the deep aquifer becomes even more difficult to be achieved in a limited time period. The effect of the bedrock blocking was demonstrated by the temporal velocity profile across the dashed line of AA', which was divided by the Huqiu bedrock (HQ Rock) (Fig. 12c). In early 1993, large settlement rates (16 cm/yr) were observed on both sides of the HQ bedrock. However, the faster decaying settlement in the downtown did not extend to the neighboring districts that are close enough to the northwest side of the HQ bedrock. Locations in the northern HQ and western XC require extra about 4.5

years compared to the areas in the east side to reach a reasonable rate, say, 10 mm/yr (Fig. 12c). Therefore, the effects from spatially irregular pumping and bedrock blocking can jointly explain the formation of the distinctive boundary between the red patches and blue corridor (Fig. 12a).

Fig. 12b summarized the histogram and the PDF (probability density function) curve of the time estimates. At a 95% confidence level, it requires 10.5 ± 0.9 years, i.e., in $2006_{-0.4}^{+1.4}$, to achieve a reasonable land settlement for the entire city. To intuitively understand the surface recovery process of Suzhou, readers are referred to the dynamic description of supplementary Gif. S1, which shows the variation of normalized subsidence rates (from -1 to 0 , with -1 being the largest subsidence rate of the entire area) at different time spots. Given the insufficient geodetic and hydrological observations, Fig. 12a provides an alternative solution for evaluating the RGE policy and for planning water resource management.

5. Concluding remarks

In this study, we investigated the spatiotemporal behaviors of water pumping related urban subsidence in Suzhou and the ground displacement response to the RGE policy. The hybrid SBAS and integrated PS and DS methods help retrieve the long-term ground deformation from 1993 to 2010 using multiple SAR sensors. The distribution of drastic subsiding zones was highlighted, coincided with the groundwater depressions. By applying the PCA on the time-series displacement, the predominant inelastic aquifer compaction, moderate shallow sediment deformation, and minor seasonal signals were separated out and interpreted. We characterized the spatially variant decaying subsidence and thus surface response to the performance of the RGE. Beyond that, we also inferred

the boundary of shallow sediments and quantified the time required for the RGE policy to take effect. The methods and analysis used in this study can be applied to the larger SWC area and other cities with similar subsidence issues. For the Suzhou case, we draw the following conclusions and implications:

1. The major subsidence area and the groundwater level depressions are well correlated. We detected evident subsidence centers in Suzhou downtown and the HQ and XC districts, with cumulative settlement of more than 0.9 m during 1993–2010. The long-term, large magnitude land subsidence was due to the inelastic compaction of the aquifer system caused by continuously decreased water level below the preconsolidation head. The RGE policy was proved to be successful in controlling the land subsidence in Suzhou. Results from the PCA analysis show that the inelastic subsidence in the city was decaying at an exponential factor of -0.147 , with the most pronounced impact in downtown. Therefore, it is believed that an effective restriction on groundwater pumping can help prevent the land deformation of the urban landscape in the future.
2. The XC and HQ districts north of downtown experienced continuous subsidence after 2003. The reason, as revealed by the nearby well observations, lies in the active water pumpage for industrial production, and thus the compressible sediments in the alluvia basin consolidate and subsidence. Although, a prompt control of water pumping helped recover the groundwater level and decelerate the land subsidence, some local areas still experienced water pumping and the land subsidence continued. To avoid the formation of secondary settlement centers like the downtown, adherence to the RGE policy is important and warranted.
3. Subsurface boundaries of the sharp bedrock gradient were identified around the outcrop area between T.H. lake and downtown, the Huqiu outcrop area, and in the north of the imaged region (Fig. 10a). The inferred boundaries have been confidently validated by a good consistency with the isobath map (Zhang et al., 2016). Benefiting from the fine resolution of InSAR measurements, we were able to map out detailed and accurate boundaries, which updated our knowledge on the potential shallow bedrocks that were not identified in historic, rough contour lines. These implications directly serve for urban planning and civil engineering, especially for the underground construction.
4. An elongated corridor connects the southeast corner of T.H. lake and the Y.C. lake, which was found to have the shortest time response (~ 9.5 years) of subsidence deceleration to the implementation of RGE. Additional random pumpage, irregular bedrock topography, and the heterogeneous aquifer units jointly contribute to the spatiotemporal varying deformation behaviors. In general, XC and HQ districts have a longer time response, whereas the downtown and areas in the vicinity to the open water bodies have a shorter time response. The statistics suggest that the continuous subsidence in Suzhou due to groundwater overexploitation has been effectively controlled around the year $2006_{-0.4}^{+1.4}$. This quantitative approach presented in this study can help better evaluate the effectiveness of the RGE policy and forecast the development for future plans in a systematic framework.

Declaration of Competing Interest

The authors declare that they have no known competing financial interests or personal relationships that could have appeared to influence the work reported in this paper.

Acknowledgement

We thank the anonymous reviewers and the editor for their helpful comments and suggestions. The first author acknowledges the fruitful discussions with Prof. Roland Bürgmann from UC Berkeley. This work

was supported by the Research Grants Council of the Hong Kong Special Administrative Region, China (AoE/E-603/18, CUHK14504219), the National Key R&D Program of China (2019YFC1510400), the National Natural Science Foundation of China (41971278), the Global Scholarship Programme for Research Excellence, the Chinese University of Hong Kong. ERS-1/2 and Envisat-ASAR data were provided by the Europe Space Agency (ESA), and ALOS-1 data were provided by Japan Aerospace Exploration Agency (JAXA). Water well observations were provided by the Hydrology and Water Resources investigation Bureau of Jiangsu. Monthly lake level and precipitation were obtained from Taihu Basin Authority and Bureau of Statistics, Jiangsu Province, respectively.

Appendix A. Supplementary data

Supplementary data to this article can be found online at <https://doi.org/10.1016/j.rse.2021.112327>.

References

- Abidin, H., Andreas, H., Gumilar, I., Brinkman, J., 2015. Study on the risk and impacts of land subsidence in Jakarta. *Proc. Int. Assoc. Hydrol. Sci.* 372, 115–120. <https://doi.org/10.5194/piahs-372-115-2015>.
- Abir, I., Khan, S., Ghulam, A., Tariq, S., Shah, M., 2015. Active tectonics of western Potwar Plateau–Salt Range, northern Pakistan from InSAR observations and seismic imaging. *Remote Sens. Environ.* 168, 265–275. <https://doi.org/10.1016/j.rse.2015.07.011>.
- Ardizzone, F., Rossi, M., Calò, F., Paglia, L., Manunta, M., Mondini, A., Zeni, G., Reichenbach, P., Lanari, R., Guzzetti, F., 2011. Preliminary analysis of a correlation between ground deformations and rainfall: the Ivanchich landslide, Central Italy. *Proc. SPIE* 8179, 81790L. <https://doi.org/10.1117/12.899453>.
- Bell, J., Amelung, F., Ferretti, A., Bianchi, M., Novali, F., 2008. Permanent scatterer InSAR reveals seasonal and long-term aquifer system response to groundwater pumping and artificial recharge. *Water Resour. Res.* 44 (2), 282–288. <https://doi.org/10.1029/2007wr006152>.
- Berardino, P., Fornaro, G., Lanari, R., Sansosti, E., 2002. A new algorithm for surface deformation monitoring based on small baseline differential SAR interferograms. *IEEE Trans. Geosci. Remote Sens.* 40 (11), 2375–2383. <https://doi.org/10.1109/TGRS.2002.803792>.
- Besse, P., 1992. PCA stability and choice of dimensionality. *Stat. Probab. Lett.* 13 (5), 405–410. [https://doi.org/10.1016/0167-7152\(92\)90115-L](https://doi.org/10.1016/0167-7152(92)90115-L).
- Besse, P., de Falguerolles, A., 1993. Application of resampling methods to the choice of dimension in principal component analysis. *Computer intensive methods in statistics*. Physica, Heidelberg 1993, 167–176. https://doi.org/10.1007/978-3-642-52468-4_11.
- Bürgmann, R., Hilley, G., Ferretti, A., Novali, F., 2006. Resolving vertical tectonics in the San Francisco Bay Area from permanent scatterer InSAR and GPS analysis. *Geology* 34 (3), 221–224. <https://doi.org/10.1130/G22064.1>.
- Calabro, M., Schmidt, D., Roering, J., 2010. An examination of seasonal deformation at the Portuguese bend landslide, southern California, using radar interferometry. *J. Geophys. Res. Earth Surf.* 115 (F2) <https://doi.org/10.1029/2009JF001314>.
- Casu, F., Manzo, M., Lanari, R., 2006. A quantitative assessment of the SBAS algorithm performance for surface deformation retrieval from DInSAR data. *Remote Sens. Environ.* 102 (3–4), 195–210. <https://doi.org/10.1016/j.rse.2006.01.023>.
- Chaussard, E., Amelung, F., Abidin, H., Hong, S., 2013. Sinking cities in Indonesia: ALOS PALSAR detects rapid subsidence due to groundwater and gas extraction. *Remote Sens. Environ.* 128, 150–161. <https://doi.org/10.1016/j.rse.2012.10.015>.
- Chaussard, E., Bürgmann, R., Shirzaei, M., Fiielding, E., Baker, B., 2014a. Predictability of hydraulic head changes and characterization of aquifer-system and fault properties from InSAR-derived ground deformation. *J. Geophys. Res. Solid Earth* 119 (8), 6572–6590. <https://doi.org/10.1002/2014JB011266>.
- Chaussard, E., Wdowinski, S., Cabral-Cano, E., Amelung, F., 2014b. Land subsidence in Central Mexico detected by ALOS InSAR time-series. *Remote Sens. Environ.* 140, 94–106. <https://doi.org/10.1016/j.rse.2013.08.038>.
- Chen, X., Hu, Q., 2004. Groundwater influences on soil moisture and surface evaporation. *J. Hydrol.* 297 (1–4), 285–300. <https://doi.org/10.1016/j.jhydrol.2004.04.019>.
- Chen, C., Pei, S., Jiao, J., 2003. Land subsidence caused by groundwater exploitation in Suzhou City, China. *Hydrogeol. J.* 11 (2), 275–287. <https://doi.org/10.1007/s10040-002-0225-5>.
- Chen, J., Knight, R., Zebker, H., Schreider, W., 2016. Confined aquifer head measurements and storage properties in the San Luis Valley, Colorado, from spaceborne InSAR observations. *Water Resour. Res.* 52 (5), 3623–3636. <https://doi.org/10.1002/2015wr018466>.
- Cigna, F., Osmanoglu, B., Cabral-Cano, E., Dixon, T., Ávila-Olivera, J., Garduño-Monroy, V., DeMets, C., Wdowinski, S., 2012. Monitoring land subsidence and its induced geological hazard with synthetic aperture radar interferometry: a case study in Morelia, Mexico. *Remote Sens. Environ.* 117, 146–161. <https://doi.org/10.1016/j.rse.2011.09.005>.

- Cigna, F., Bianchini, S., Casagli, N., 2013. How to assess landslide activity and intensity with persistent Scatterer interferometry (PSI): the PSI-based matrix approach. *Landslides* 10 (3), 267–283. <https://doi.org/10.1007/s10346-012-0335-7>.
- Cohen-Waeber, J., Bürgmann, R., Chaussard, E., Giannico, C., Ferretti, A., 2018. Spatiotemporal patterns of precipitation-modulated landslide deformation from independent component analysis of InSAR time series. *Geophys. Res. Lett.* 45 (4), 1878–1887. <https://doi.org/10.1002/2017GL075950>.
- Crosetto, M., Monserrat, O., Cuevas-González, M., Devanthery, N., Crippa, B., 2016. Persistent scatterer interferometry: a review. *ISPRS J. Photogramm. Remote Sens.* 115, 78–89. <https://doi.org/10.1016/j.isprsjprs.2015.10.011>.
- Dong, J., Zhang, L., Tang, M., Liao, M., Xu, Q., Gong, J., Ao, M., 2017. Mapping landslide surface displacements with time series SAR interferometry by combining persistent and distributed scatterers: a case study of Jiayu landslide in Danba, China. *Remote Sens. Environ.* 205, 180–198. <https://doi.org/10.1016/j.rse.2017.11.022>.
- Ferretti, A., Prati, C., Rocca, F., 2001. Permanent scatterers in SAR interferometry. *IEEE Trans. Geosci. Remote Sens.* 39 (1), 8–20. <https://doi.org/10.1109/36.898661>.
- Ferretti, A., Fumagalli, A., Novali, F., Prati, C., Rocca, F., Rucci, A., 2011. A new algorithm for processing interferometric data-stacks: SqueeSAR. *IEEE Trans. Geosci. Remote Sens.* 49 (9), 3460–3470. <https://doi.org/10.1109/TGRS.2011.2124465>.
- Foster, S., 2001. The interdependence of groundwater and urbanisation in rapidly developing cities. *Urban Water* 3 (3), 185–192. [https://doi.org/10.1016/S1462-0758\(01\)00043-7](https://doi.org/10.1016/S1462-0758(01)00043-7).
- Foster, S., Morris, B., Chilton, P., 1999. *Groundwater in urban development—a review of linkages and concerns*. IAHS Publ. 1999, 3–12.
- Galloway, D., Hudnut, K., Ingebritsen, S., Phillips, S., Peltzer, G., Rogez, F., Rosen, P., 1998. Detection of aquifer system compaction and land subsidence using interferometric synthetic aperture radar, Antelope Valley, Mojave Desert, California. *Water Resour. Res.* 34 (10), 2573–2585. <https://doi.org/10.1029/98WR01285>.
- Gerbrands, J., 1981. On the relationships between SVD, KLT and PCA. *Pattern Recogn.* 14 (1–6), 375–381. [https://doi.org/10.1016/0031-3203\(81\)90082-0](https://doi.org/10.1016/0031-3203(81)90082-0).
- Gong, W., Zhang, J., Zhang, Y., 2008. Detecting ground deformation with permanent scatterer of Suzhou region. In: 2008 International Workshop on Earth Observation and Remote Sensing Applications. IEEE, pp. 1–5. <https://doi.org/10.1109/EORSA.2008.4620304>.
- Gong, H., Pan, Y., Zheng, L., Li, X., Zhu, L., Zhang, C., Huang, Z., Li, Z., Wang, H., Zhou, C., 2018. Long-term groundwater storage changes and land subsidence development in the North China Plain (1971–2015). *Hydrogeol. J.* 26 (5), 1417–1427. <https://doi.org/10.1007/s10040-018-1768-4>.
- Guo, H., Zhang, Z., Cheng, G., Li, W., Li, T., Jiao, J., 2015. Groundwater-derived land subsidence in the North China Plain. *Environ. Earth Sci.* 74 (2), 1415–1427. <https://doi.org/10.1007/s12665-015-4131-2>.
- Haghighi, M., Motagh, M., 2019. Ground surface response to continuous compaction of aquifer system in Tehran, Iran: results from a long-term multi-sensor InSAR analysis. *Remote Sens. Environ.* 221, 534–550. <https://doi.org/10.1016/j.rse.2018.11.003>.
- Hoffmann, J., Galloway, D., Zebker, H., 2003. Inverse modeling of interbed storage parameters using land subsidence observations, Antelope Valley, California. *Water Resour. Res.* 39 (2) <https://doi.org/10.1029/2001WR001252>.
- Hooper, A., Zebker, H., Segall, P., Kampes, B., 2004. A new method for measuring deformation on volcanoes and other natural terrains using InSAR persistent scatterers. *Geophys. Res. Lett.* 31 (23) <https://doi.org/10.1029/2004GL021737>.
- Hu, R., Yue, Z., Wang, L., Wang, S., 2004. Review on current status and challenging issues of land subsidence in China. *Eng. Geol.* 76 (1–2), 65–77. <https://doi.org/10.1016/j.enggeo.2004.06.006>.
- Hu, X., Oommen, T., Lu, Z., Wang, T., Kim, J.W., 2017. Consolidation settlement of salt Lake County tailings impoundment revealed by time-series InSAR observations from multiple radar satellites. *Remote Sens. Environ.* 202, 199–209. <https://doi.org/10.1016/j.rse.2017.05.023>.
- Hu, X., Lu, Z., Wang, T., 2018. Characterization of hydrogeological properties in Salt Lake Valley, Utah using InSAR. *J. Geophys. Res. Earth Surf.* 123. <https://doi.org/10.1029/2017JF004497>.
- Hu, X., Bürgmann, R., Lu, Z., Handwerker, A., Wang, T., Miao, R., 2019. Mobility, thickness, and hydraulic diffusivity of the slow-moving Monroe landslide in California revealed by L-band satellite radar interferometry. *J. Geophys. Res. Solid Earth* 124 (7), 7504–7518. <https://doi.org/10.1029/2019JB017560>.
- Huang, Y., Zhou, Z., 2011. Effect analysis after prohibition of pumping groundwater in Su-xi-Chang area of China. In: 2011 Second International Conference on Mechanic Automation and Control Engineering. IEEE, pp. 7326–7329. <https://doi.org/10.1109/MACE.2011.5988741>.
- Huang, F., Wang, G., Yang, Y., Wang, C., 2014. Overexploitation status of groundwater and induced geological hazards in China. *Nat. Hazards* 73 (2), 727–741. <https://doi.org/10.1007/s11069-014-1102-y>.
- Ji, K., Herring, T., 2011. Transient signal detection using GPS measurements: transient inflation at Akutan volcano, Alaska, during early 2008. *Geophys. Res. Lett.* 38 (6) <https://doi.org/10.1029/2011GL046904>.
- Jiang, L., Bai, L., Zhao, Y., Cao, G., Wang, H., Sun, Q., 2018. Combining InSAR and hydraulic head measurements to estimate aquifer parameters and storage variations of confined aquifer system in Cangzhou, North China Plain. *Water Resour. Res.* 54, 8234–8252. <https://doi.org/10.1029/2017WR022126>.
- Johnson, B., Albani, A., Rickwood, P., Tayton, J., 1977. The bedrock topography of the botany basin, New South Wales. *J. Geol. Soc. Aust.* 24 (7–8), 403–408. <https://doi.org/10.1080/00167617708728998>.
- Li, Y., Guo, Y., Yu, G., 2013. An analysis of extreme flood events during the past 400 years at Taihu Lake, China. *J. Hydrol.* 500, 217–225. <https://doi.org/10.1016/j.jhydrol.2013.02.028>.
- Li, G., Lin, H., Ye, Q., 2018. Heterogeneous decadal glacier downwasting at the Mt. Everest (Qomolangma) from 2000 to~ 2012 based on multi-baseline bistatic SAR interferometry. *Remote Sens. Environ.* 206, 336–349. <https://doi.org/10.1016/j.rse.2017.12.032>.
- Lin, Y., Kositsky, A., Avouac, J., 2010. PCAIM joint inversion of InSAR and ground-based geodetic time series: application to monitoring magmatic inflation beneath the Long Valley caldera. *Geophys. Res. Lett.* 37 (23) <https://doi.org/10.1029/2010GL045769>.
- Lischeid, G., 2009. Non-linear visualization and analysis of large water quality data sets: a model-free basis for efficient monitoring and risk assessment. *Stoch. Env. Res. Risk* A. 23 (7), 977–990. <https://doi.org/10.1007/s00477-008-0266-y>.
- Liu, H., Zhang, D., Wang, B., 2008. Daily to submonthly weather and climate characteristics of the summer 1998 extreme rainfall over the Yangtze River basin. *J. Geophys. Res.-Atmos.* 113 (D22) <https://doi.org/10.1029/2008JD010072>.
- Lophaven, S., Nielsen, H., Sondergaard, J., 2002. DACE: a Matlab Kriging toolbox, version 2.0. IMM Technical University of Denmark, Lyngby. <http://www.omicron.dk/dace.html>.
- Lyu, H., Xu, Y., Cheng, W., et al., 2018. Flooding hazards across southern China and prospective sustainability measures. *Sustainability* 10 (5), 1682. <https://doi.org/10.3390/su10051682>.
- Ma, P., Lin, H., 2016. Robust detection of single and double persistent scatterers in urban built environments. *IEEE Trans. Geosci. Remote Sens.* 54 (4), 2124–2139. <https://doi.org/10.1109/TGRS.2015.2496193>.
- Ma, P., Lin, H., Lan, H., Chen, F., 2015. Multi-dimensional SAR tomography for monitoring the deformation of newly built concrete buildings. *ISPRS J. Photogramm. Remote Sens.* 106, 118–128. <https://doi.org/10.1016/j.isprsjprs.2015.04.012>.
- Meadows, P., Rosich-Tell, B., Santella, C., 2005. The ERS-2 SAR performance: the first 9 years. *Envisat . ERS Symp.* 2005, 572. <http://adsabs.harvard.edu/full/2005ESASP.572E...3M>.
- Miller, M., Shirzaei, M., Argus, D., 2017. Aquifer mechanical properties and decelerated compaction in Tucson, Arizona. *J. Geophys. Res. Solid Earth* 122, 8402–8416. <https://doi.org/10.1002/2017JB014531>.
- Miranda, N., Rosich, B., Santella, C., Grison, M., 2005. Review of the impact of ERS-2 piloting modes on the SAR Doppler stability. In: *Envisat & ERS Symposium*. 572. <http://adsabs.harvard.edu/full/2005ESASP.572E...4M>.
- Mohr, J., Reeh, N., Madsen, S., 1998. Three-dimensional glacial flow and surface elevation measured with radar interferometry. *Nature* 391 (6664), 273. <https://doi.org/10.1038/34635>.
- Ng, C., Liu, G., Li, Q., 2013. Investigation of the long-term tunnel settlement mechanisms of the first metro line in Shanghai. *Can. Geotech. J.* 50 (6), 674–684. <https://doi.org/10.1139/cgj-2012-0298>.
- Novakowski, K., Gillham, R., 1988. Field investigations of the nature of water-table response to precipitation in shallow water-table environments. *J. Hydrol.* 97 (1–2), 23–32. [https://doi.org/10.1016/0022-1694\(88\)90063-7](https://doi.org/10.1016/0022-1694(88)90063-7).
- Osmanoglu, B., Dixon, T., Wdowinski, S., Cabral-Cano, E., Jiang, Y., 2011. Mexico City subsidence observed with persistent scatterer InSAR. *Int. J. Appl. Earth Obs. Geoinf.* 13 (1), 1–12. <https://doi.org/10.1016/j.jag.2010.05.009>.
- Pacheco-Martínez, J., Hernández-Marín, M., Burbey, T., González-Cervantes, N., Ortíz-Lozano, J., Zermeno-De-Leon, M., Solís-Pinto, A., 2013. Land subsidence and ground failure associated to groundwater exploitation in the Aguascalientes Valley, México. *Eng. Geol.* 2013 (164), 172–186. <https://doi.org/10.1016/j.enggeo.2013.06.015>.
- Qin, X., Zhang, L., Yang, M., Luo, H., Liao, M., Ding, X., 2018. Mapping surface deformation and thermal dilation of arch bridges by structure-driven multi-temporal DInSAR analysis. *Remote Sens. Environ.* 216, 71–90. <https://doi.org/10.1016/j.rse.2018.06.032>.
- Richman, M., 1986. Rotation of principal components. *J. Climatol.* 6 (3), 293–335. <https://doi.org/10.1002/joc.3370060305>.
- Rucci, A., Ferretti, A., Guarnieri, A.M., Rocca, F., 2012. Sentinel 1 SAR interferometry applications: the outlook for sub millimeter measurements. *Remote Sens. Environ.* 120, 156–163. <https://doi.org/10.1016/j.rse.2011.09.030>.
- Rudolph, M., Shirzaei, M., Manga, M., Fukushima, Y., 2013. Evolution and future of the Lusi mud eruption inferred from ground deformation. *Geophys. Res. Lett.* 40 (6), 1089–1092. <https://doi.org/10.1002/grl.50189>.
- Samsonov, S., 2010. Topographic correction for ALOS PALSAR interferometry. *IEEE Trans. Geosci. Remote Sens.* 48 (7), 3020–3027. <https://doi.org/10.1109/TGRS.2010.2043739>.
- Shi, X., Xue, Y., Ye, S., Wu, J., Zhang, Y., Yu, J., 2007. Characterization of land subsidence induced by groundwater withdrawals in Su-Xi-Chang area, China. *Environ. Geol.* 52 (1), 27. <https://doi.org/10.1007/s00254-006-0446-3>.
- Shi, X., Wu, J., Ye, S., Zhang, Y., Xue, Y., Wei, Z., Li, Q., Yu, J., 2008a. Regional land subsidence simulation in Su-Xi-Chang area and Shanghai city, China. *Eng. Geol.* 100 (1–2), 27–42. <https://doi.org/10.1016/j.enggeo.2008.02.011>.
- Shi, X., Xue, Y., Wu, J., Ye, S., Zhang, Y., Wei, Z., Yu, J., 2008b. Characterization of regional land subsidence in Yangtze Delta, China: the example of Su-Xi-Chang area and the city of Shanghai. *Hydrogeol. J.* 16 (3), 593–607. <https://doi.org/10.1007/s10040-007-0237-2>.
- Shi, X., Fang, R., Wu, J., Xu, H., Sun, Y., Yu, J., 2012. Sustainable development and utilization of groundwater resources considering land subsidence in Suzhou, China. *Eng. Geol.* 124, 77–89. <https://doi.org/10.1016/j.enggeo.2011.10.005>.
- Shi, G., He, X., Xiao, B., 2015. Acquiring three-dimensional deformation of Kilauea's south flank from GPS and DInSAR integration based on the ant colony optimization. *IEEE Geosci. Remote Sens. Lett.* 12 (12), 2506–2510. <https://doi.org/10.1109/LGRS.2015.2489243>.
- Shi, G., Lin, H., Ma, P., 2018. A hybrid method for stability monitoring in low-coherence urban regions using persistent and distributed scatterers. *IEEE J. Select. Top. Appl. Earth Observ. Remote Sens.* 11 (10), 3811–3821. <https://doi.org/10.1109/JSTARS.2018.2867832>.

- Shi, G., Lin, H., Bürgmann, R., Ma, P., Wang, J., Liu, Y., 2019. Early soil consolidation from magnetic extensometers and full resolution SAR interferometry over highly decorrelated reclaimed lands. *Remote Sens. Environ.* 231, 111231. <https://doi.org/10.1016/j.rse.2019.111231>.
- Sun, W., 2002. Investigation report on prevention and control of land subsidence in Yangtze Delta (in Chinese). In: *Proceedings of the National Symposium on Land Subsidence*. Shanghai Institute of Geology Survey, Shanghai, pp. 1–12.
- Terzaghi, K., 1925. *Principles of soil mechanics, IV: settlement and consolidation of clay*. *Eng. News-Rec.* 95 (3), 874–878.
- Townley, L., Trefry, M., 2000. Surface water-groundwater interaction near shallow circular lakes: flow geometry in three dimensions. *Water Resour. Res.* 36 (4), 935–948. <https://doi.org/10.1029/1999WR900304>.
- van der Horst, T., Rutten, M., van de Giesen, N., Hanssen, R., 2018. Monitoring land subsidence in Yangon, Myanmar using Sentinel-1 persistent scatterer interferometry and assessment of driving mechanisms. *Remote Sens. Environ.* 217, 101–110. <https://doi.org/10.1016/j.rse.2018.08.004>.
- Wang, G., You, G., Shi, B., Yu, J., Li, H., Zong, K., 2009. Earth fissures triggered by groundwater withdrawal and coupled by geological structures in Jiangsu Province, China. *Environ. Geol.* 57 (5), 1047–1054. <https://doi.org/10.1007/s00254-008-1390-1>.
- Wang, L., Cai, Y., Chen, H., Dag, D., Zhao, J., Yang, J., 2011. Flood disaster in Taihu Basin, China: causal chain and policy option analyses. *Environ. Earth Sci.* 63 (5), 1119–1124. <https://doi.org/10.1007/s12665-010-0786-x>.
- Wang, Y., Zhu, X., Zeisl, B., Pollefeys, M., 2016. Fusing meter-resolution 4-D InSAR point clouds and optical images for semantic urban infrastructure monitoring. *IEEE Trans. Geosci. Remote Sens.* 55 (1), 14–26. <https://doi.org/10.1109/TGRS.2016.2554563>.
- Wang, T., Shi, Q., Nikkhoo, M., Wei, S., Barbot, S., Dreger, D., Bürgmann, R., Motagh, M., Chen, Q., 2018. The rise, collapse, and compaction of Mt. Mantap from the 3 September 2017 North Korean nuclear test. *Science* 361 (6398), 166–170. <https://doi.org/10.1126/science.aar7230>.
- Wang, Y., Wang, Z., Cheng, W., 2019. A review on land subsidence caused by groundwater withdrawal in Xi'an, China. *Bull. Eng. Geol. Environ.* 78 (4), 2851–2863. <https://doi.org/10.1007/s10064-018-1278-6>.
- Wu, T., 2000. 1999 catastrophic flood in Taihu Basin and the consideration for Taihu flood control planning (in Chinese). *J. Lake Sci.* 2000 (1), 1. <https://doi.org/10.18307/2000.0102>.
- Wu, J., Shi, X., Xue, Y., Zhang, Y., Wei, Z., Yu, J., 2008. The development and control of the land subsidence in the Yangtze Delta, China. *Environ. Geol.* 55 (8), 1725–1735. <https://doi.org/10.1007/s00254-007-1123-x>.
- Wu, J., Shi, X., Ye, S., Xue, Y., Zhang, Y., Yu, J., 2009. Numerical simulation of land subsidence induced by groundwater overexploitation in Su-Xi-Chang area, China. *Environ. Geol.* 57 (6), 1409–1421. <https://doi.org/10.1007/s00254-008-1419-5>.
- Xu, B., Feng, G., Li, Z., Wang, Q., Wang, C., Xie, R., 2016. Coastal subsidence monitoring associated with land reclamation using the point target based SBAS-InSAR method: a case study of Shenzhen, China. *Remote Sens.* 8 (8), 652. <https://doi.org/10.3390/rs8080652>.
- Xue, Y., Zhang, Y., Ye, S., Wu, J., Li, Q., 2005. Land subsidence in China. *Environ. Geol.* 48 (6), 713–720. <https://doi.org/10.1007/s00254-005-0010-6>.
- Yan, H., 1998. Analysis on the weather and climate features and causes of the extraordinary flood disaster over China in 1998 and the relevant meteorological prediction services (in Chinese). *Climat. Environ. Res.* 3, 323–334.
- Ye, S., Franceschini, A., Zhang, Y., Janna, C., Gong, X., Yu, J., Teatini, P., 2018. A novel approach to model earth fissure caused by extensive aquifer exploitation and its application to the Wuxi case, China. *Water Resour. Res.* 54 (3), 2249–2269. <https://doi.org/10.1002/2017WR021872>.
- Yu, J., Wang, X., Wu, J., Xie, J., 2006. Characteristics of land subsidence and its remedial proposal in Suzhou-Wuxi-Changzhou area (in Chinese). *Geol. J. China Univ.* 12 (2), 179–184. <https://doi.org/10.3969/j.issn.1006-7493.2006.02.004>.
- Yuan, M., Zhou, W., 2001. Ground subsidence disaster and origin analysis in Suzhou (in Chinese). *J. Geol. Haz. Environ. Preserv.* 12 (2) <https://doi.org/10.3969/j.issn.1006-4362.2001.02.006>.
- Zhang, L., Roger, C., Wu, C., 2003. Land subsidence problem and its control in Taihu Basin of South Jiangsu Province due to overexploitation of underground water (in Chinese). *J. Lake Sci.* 15 (3), 257–262. <https://doi.org/10.18307/2003.0310>.
- Zhang, Y., Xue, Y., Wu, J., Ye, S., Wei, Z., Li, Q., Yu, J., 2007. Characteristics of aquifer system deformation in the southern Yangtze Delta, China. *Eng. Geol.* 90 (3–4), 160–173. <https://doi.org/10.1016/j.enggeo.2007.01.004>.
- Zhang, Y., Xue, Y., Wu, J., Shi, X., Yu, J., 2010. Excessive groundwater withdrawal and resultant land subsidence in the Su-Xi-Chang area, China. *Environ. Earth Sci.* 61 (6), 1135–1143. <https://doi.org/10.1007/s12665-009-0433-6>.
- Zhang, Y., Zhang, J., Wu, H., Lu, Z., Guangtong, S., 2011. Monitoring of urban subsidence with SAR interferometric point target analysis: a case study in Suzhou, China. *Int. J. Appl. Earth Obs. Geoinf.* 13 (5), 0–818. <https://doi.org/10.1016/j.jag.2011.05.003>.
- Zhang, Y., Wang, Z., Xue, Y., Wu, J., Yu, J., 2016. Mechanisms for earth fissure formation due to groundwater extraction in the Su-Xi-Chang area, China. *Bull. Eng. Geol. Environ.* 75 (2), 745–760. <https://doi.org/10.1007/s10064-015-0775-0>.
- Zhou, C., Gong, H., Zhang, Y., Warner, T., Wang, C., 2018. Spatiotemporal evolution of land subsidence in the Beijing plain 2003–2015 using persistent scatterer interferometry (PSI) with multi-source SAR data. *Remote Sens.* 10 (4), 552. <https://doi.org/10.3390/rs10040552>.
- Zhou, L., Ma, P., Xia, Y., Gong, S., 2019. Deformation monitoring and analysis of the thermal expansion of high-rise buildings in Shanghai Lujiazui using tomography-based persistent scatterer interferometry. *J. Appl. Remote Sens.* 13 (4), 044517. <https://doi.org/10.1117/1.JRS.13.044517>.
- Zhu, X., Yu, J., Wu, J., 2006. Prediction of ground fissures in Suzhou-Wuxi-Changzhou area based on ANN analysis (in Chinese). *Chinese J. Geol. Haz. Control* 2006, 2.
- Zong, Y., Chen, X., 2000. The 1998 flood on the Yangtze, China. *Nat. Hazards* 22 (2), 165–184. <https://doi.org/10.1023/A:1008119805106>.